

RESEARCH ARTICLE

Ciona embryonic tail bending is driven by asymmetrical notochord contractility and coordinated by epithelial proliferation

Qiongxuan Lu^{1,2,3,*}, Yuan Gao^{4,*}, Yuanyuan Fu^{1,2}, Hongzhe Peng¹, Wenjie Shi¹, Bo Li⁴, Zhiyi Lv^{1,2,3}, Xi-Qiao Feng⁴ and Bo Dong^{1,2,3,†}

ABSTRACT

Ventral bending of the embryonic tail within the chorion is an evolutionarily conserved morphogenetic event in both invertebrates and vertebrates. However, the complexity of the anatomical structure of vertebrate embryos makes it difficult to experimentally identify the mechanisms underlying embryonic folding. This study investigated the mechanisms underlying embryonic tail bending in chordates. To further understand the mechanical role of each tissue, we also developed a physical model with experimentally measured parameters to simulate embryonic tail bending. Actomyosin asymmetrically accumulated at the ventral side of the notochord, and cell proliferation of the dorsal tail epidermis was faster than that in the ventral counterpart during embryonic tail bending. Genetic disruption of actomyosin activity and inhibition of cell proliferation dorsally caused abnormal tail bending, indicating that both asymmetrical actomyosin contractility in the notochord and the discrepancy of epidermis cell proliferation are required for tail bending. In addition, asymmetrical notochord contractility was sufficient to drive embryonic tail bending, whereas differential epidermis proliferation was a passive response to mechanical forces. These findings showed that asymmetrical notochord contractility coordinates with differential epidermis proliferation mechanisms to drive embryonic tail bending.

This article has an associated 'The people behind the papers' interview.

KEY WORDS: *Ciona*, Embryonic bending, Actomyosin contractility, Cell proliferation, Physical model

INTRODUCTION

Tissue bending and folding, including the formation of the vertebrate neural tube, the germ layer (during gastrulation) and the gut, are essential evolutionarily conserved morphogenetic processes in embryogenesis. However, coupled bending-folding processes also occur on a large scale beyond the tissue level, such as embryonic folding. In vertebrates, embryonic folding changes a disc-like embryo into a curved, cylindrical-shaped one (Tuchmann-

Duplessis et al., 1971). Embryonic folding includes longitudinal folding, which produces both head and tail folds, and transverse folding, which produces right and left lateral folds. Failure in any of the bending-folding processes leads to severe birth defects (e.g. craniorachischisis) (Copp and Greene, 2013).

Various mechanisms underlie tissue bending and/or folding in both invertebrates and vertebrates. For example, actomyosin-mediated apical constriction [narrowing at the apical surface of the cell (Lv et al., 2019)] is required for gastrulation in *Drosophila melanogaster*, *Caenorhabditis elegans* and *Ciona intestinalis* (Lee and Goldstein, 2003; Martin et al., 2009; Sherrard et al., 2010) and vertebrate neural tube formation (Haigo et al., 2003; Nishimura et al., 2012). Similarly, basal constriction (narrowing at the basal surface of the cell) is required for the formation of the zebrafish optic cup (Nicolás-Pérez et al., 2016) and the midbrain-hindbrain boundary (Gutzman et al., 2008). Differential growth, due to increased cell proliferation or volume in one layer of cells relative to an adjacent layer, is another important mechanism responsible for tissue bending and folding. For example, hinged folding in the avian gut endoderm is driven by localized differential epidermis proliferation (Miller et al., 1999), whereas chick embryonic heart bending is due to differential hypertrophic growth (Shi et al., 2014).

In addition to these mechanisms, cell apoptosis (Monier et al., 2015), cell mitotic rounding (Kondo and Hayashi, 2013) and differential positioning of the adherens junction (Wang et al., 2012) also contribute to tissue bending and/or folding. Increasing evidence shows that most of the tissue-bending and tissue-folding processes are driven by the interaction of multiple mechanisms. For example, both basal actomyosin constriction and active epithelial migration are required for retinal neuroepithelium bending during zebrafish optic cup morphogenesis (Sidhaye and Norden, 2017), and both cell adhesion and differences in tissue growth are required for the folding during early tooth germ formation (Marin-Riera et al., 2018).

Although tissue bending has been extensively studied at the tissue level, the mechanisms that sculpt the tissue-bending and tissue-folding morphology at the embryo scale are unclear because of anatomical complexity. We addressed this question by taking advantage of the relatively transparent, structurally simple chordate *Ciona robusta* (also called *C. intestinalis* type A) embryo, which is an ideal system for determining cellular and molecular mechanisms underlying morphogenesis at a whole-embryo scale. The notochord is responsible for both tail elongation and tail morphology because disruption of notochord intercalation or elongation leads to defects in the notochord and hence tail morphogenesis (Jose-Edwards et al., 2013; Oda-Ishii et al., 2010; Segade et al., 2016; Sehring et al., 2014; Shi et al., 2009). Cooperation between the notochord and muscle is required for tail elongation (Di Gregorio et al., 2002) and a wave-like mitotic pattern of the epidermis is crucial for tail morphogenesis during neurulation (Ogura and Sasakura, 2016). Therefore, tail morphogenesis is likely achieved via highly

¹Sars-Fang Centre, MoE Key Laboratory of Marine Genetics and Breeding, College of Marine Life Sciences, Ocean University of China, Qingdao 266003, China.

²Laboratory for Marine Biology and Biotechnology, Qingdao National Laboratory for Marine Science and Technology, Qingdao 266237, China. ³Institute of Evolution & Marine Biodiversity, Ocean University of China, Qingdao 266003, China. ⁴Institute of Biomechanics and Medical Engineering, Department of Engineering Mechanics, Tsinghua University, Beijing 100084, China.

*These authors contributed equally to this work

†Author for correspondence (bodong@ouc.edu.cn)

Q.L., 0000-0003-0233-8446; B.L., 0000-0002-3792-2469; B.D., 0000-0003-1616-5363

Handling Editor: Thomas Lecuit

Received 25 October 2019; Accepted 16 November 2020

coordinated behavior between the notochord, muscle and the epidermis. In addition to elongation, as in other species, the embryonic tail in *Ciona* bends ventrally and surrounds the trunk within the chorion. However, the underlying genetic mechanisms have not been studied because embryonic tail bending is thought to be a passive process that is achieved by the physical barrier of the chorion confining embryonic tail bending during elongation.

In this study, we experimentally investigated the mechanisms underlying embryonic tail bending in chordates. To further identify the mechanical role of each tissue, we also developed a physical model with experimentally measured parameters to simulate embryonic tail bending. Together with experiments and the biomechanical model, the findings reveal how the different tissues coordinate with each other to drive the large-scale morphogenesis at the whole-embryo scale, and provide insights into the complex embryonic bending process in chordates.

RESULTS

Ciona embryonic tail bending is under genetic control

After fertilization, *Ciona* embryos developed within a layer of membrane called the chorion (Fig. 1A, white arrowhead). The early embryo tail bent and subsequently surrounded the trunk inside the chorion (Fig. 1A; Movie 1), indicating that the tail elongates by passively bending itself down because of confinement within the chorion. Unexpectedly and excitingly, when the chorion was removed from the embryos using a chemical approach (Corbo et al., 1997), the dechorionated embryos elongated normally and still bent ventrally toward the trunk (Fig. 1A; Movie 2), although the tail-bending angle (θ) was slightly lower compared with wild-type embryos. To quantitatively evaluate the embryonic tail bending in the embryos, we plotted θ against the tail length (ζ) during tail bending (Fig. 1B). The rose diagram plots show that tail morphogenesis patterns were similar in the embryos with or without the chorion; however, θ in dechorionated embryos was lower compared with

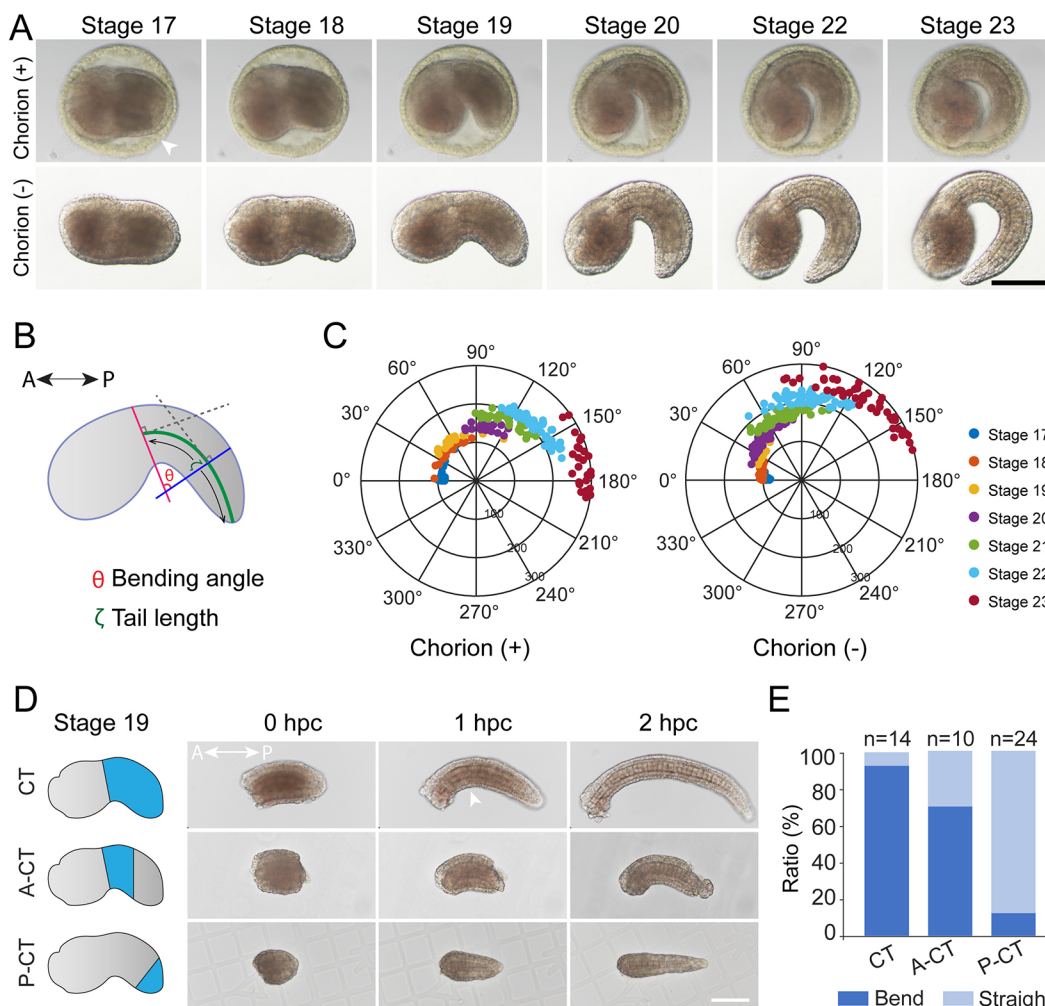


Fig. 1. *Ciona robusta* embryonic tail bending is under genetic control. (A) Snapshot images at tailbud stages 17, 18, 19, 20, 22 and 23 from time-lapse movies of *C. robusta* embryo within the chorion (+) (Movie 1) and without the chorion (-) (Movie 2). White arrowhead indicates the chorion surrounding the developing embryo. (B) Definition of the bending angle θ (cross-angle of magenta and blue lines) and tail length ζ (green line) in embryo. (C) The rose diagram plots θ and ζ of embryos within chorion (+; left) and without chorion (-; right) at tailbud stages 17-23. Each dot represents one embryo at different developmental stages (classified by colors). The diameter of the rose diagrams indicates the tail length (μm). For statistical analysis, we measured >25 embryos at each selected tailbud stage. (D) Snapshot images from time-lapse movies of tail explant experiments. All tail explants were produced from embryos at tailbud stage 19. White arrowhead indicates the maximum bending site of the tail explants. Schematic (left) shows the part of tail explant (blue) produced by needle ablation. (E) Quantification of tail-cutting experiments: 92.9% CT (13/14), 70.0% A-CT (7/10) and 12.5% P-CT (3/24) show embryonic tail-bending morphology. CT, cutting tail; A-CT, anterior cutting tail; P-CT, posterior cutting tail; hpc, hours post cutting. Scale bars: 100 μm (A); 50 μm (D).

embryos with the chorion at the same ζ (Fig. 1C). These findings showed that embryonic tail bending in *Ciona* is a chorion-independent process and controlled intrinsically by genetics.

To determine whether embryonic tail bending is autonomous, we isolated the trunk and tail parts of *Ciona* tailbud embryos at stage 19 using needle ablation, cultured the separated parts in filter-fresh seawater for 2 h and examined isolated tail fragment development (Fig. 1D, top). Surprisingly, the cutting tail (CT) bent ventrally as the tail elongated (Fig. 1D,E, $n=13/14$; Movie 3), and the maximum curvature of the bent tail was frequently located at the anterior part of the tail (Fig. 1D, white arrowhead). We further cut the isolated tail into two segments: anterior cutting tail (A-CT) and posterior cutting tail (P-CT). After 2 h post cutting, the A-CT bent ventrally ($n=7/10$) (Fig. 1D,E), whereas the P-CT did not bend but elongated straight ($n=21/24$) (Fig. 1D,E). Together, the findings indicate that embryonic tail bending in *Ciona* is an autonomous event driven by tail tissues and that the driving forces originate in the anterior part of the tail.

Actomyosin network enrichment at the notochord's ventral side in early bending embryos

The *Ciona* embryo tail comprises three main tissues: epidermis, muscle and notochord (Fig. 2A). The muscle is located symmetrically on the left and right of the tail, rather than in the dorsoventral (DV) axis (Fig. 2A, middle), so we ignored its mechanical contribution and mainly investigated the roles that the notochord and epidermis play in embryonic tail bending. Geometric analysis of notochord morphology showed that the anteroposterior (AP) length of the notochord's ventral edge was shorter compared with its dorsal edge (Fig. 2B; Table S1) at tailbud stages 17–22, indicating that the

notochord presents as a bending cylindrical shape during embryonic tail bending (Fig. 2B, inset). In addition, individual cell geometry data showed ventral narrowing of notochord cells after intercalation initiation (Fig. S1A). To determine the mechanical mechanisms underlying the ventrally bent shape, we examined the actomyosin distribution in the notochord. Longitudinal sections showed that F-actin (labeled by Phalloidin) is asymmetrically enriched at the ventral side of the notochord at tailbud stages 17–21 (Fig. 2C, $n \geq 6$; Movie 4). To avoid bias from the observed angles, we confirmed the ventral enrichment of F-actin from cross-sectional (Fig. S1B) and dorsal (Fig. S1C) views. Ventral enrichment of F-actin was more prominent at the early tailbud stage (stage 17), and the enrichment gradually became symmetrical later (tailbud stage 22) (Fig. 2C,E). Quantitative data showed that the F-actin intensity at tailbud stages 17 and 18 on the ventral side of the notochord increased by 2.5-fold compared with the dorsal side (Fig. 2E).

Nonmuscle myosin II is essential for contractility of actomyosin networks. Its motor function is activated by reversible phosphorylation of the myosin regulatory light chain (MRLC) at serine 19 and threonine 18 (Vicente-Manzanares et al., 2009). Considering results of F-actin locations (Fig. 2C), we examined active myosin II using a specific anti-pS19 MRLC antibody and found that it asymmetrically accumulated at the ventral side of the notochord during embryonic tail bending (Fig. 2D, yellow arrows, $n \geq 6$). Quantitative data further revealed that the difference between dorsal and ventral active myosin II was 1.3 times, relatively weaker compared with F-actin (Fig. 2F). Together, the findings indicate that the active actomyosin apparatus is asymmetrically located at the ventral side of the notochord, indicating that asymmetrical actomyosin contractile forces cause notochord cell shape changes.

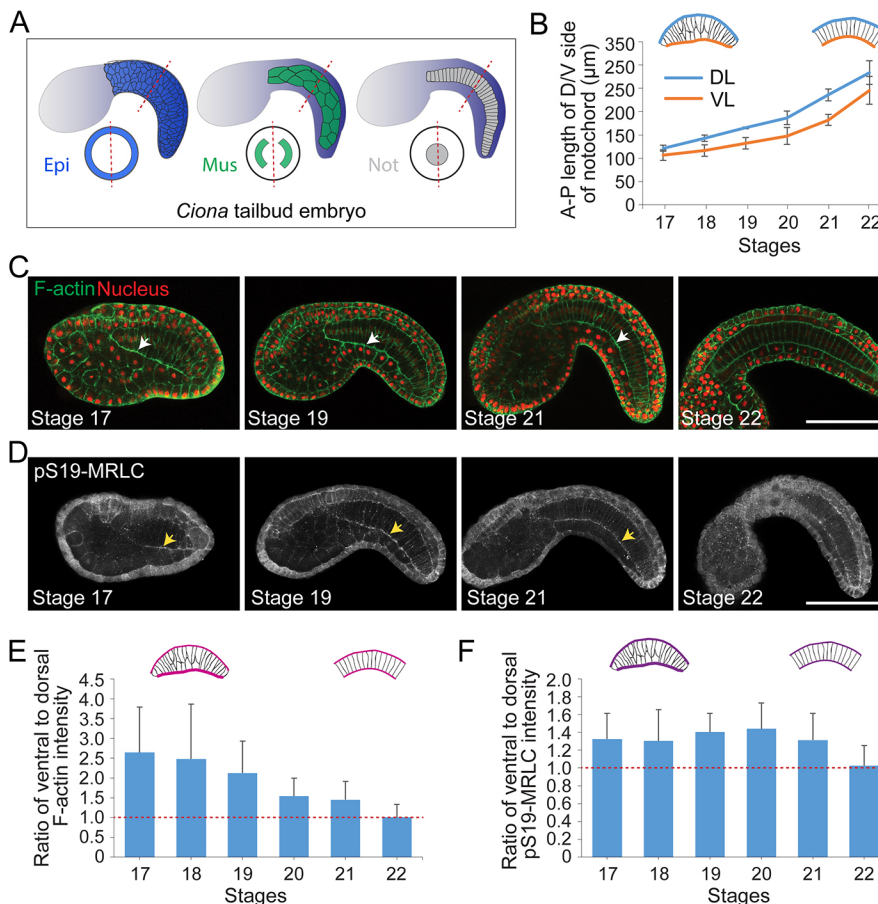


Fig. 2. Asymmetrical localization of actomyosin in the notochord during embryonic tail bending in *Ciona robusta*. (A) Sketches show longitudinal views of tail tissues of *C. robusta* embryos. Dashed red lines indicate the bending DV axis. Epi, epidermis; Mus, muscle; Not, notochord. (B) Changes in notochord geometry shown by measuring the length of the dorsal (DL) and ventral (VL) edges of the notochord. Data are mean \pm s.d. Inset shows geometry of the notochord at tailbud stages 18 and 22. (C) Confocal images of embryos labeled using Phalloidin and DAPI, showing F-actin localization (green) in the notochord at different tailbud stages (17, 19, 21 and 22) in a longitudinal view ($n=13, 12, 13$ and 6 respectively). White arrows indicate the asymmetrically enriched F-actin along the ventral side of the notochord. (D) Spatiotemporal localization of pS19-MRLC in the notochord at different tailbud stages (17, 19, 21 and 22; $n=6, 7, 6$ and 9, respectively). Yellow arrows indicate the biased pS19-MRLC accumulation along the ventral side of the notochord. (E) Quantification of ventral-to-dorsal F-actin intensity ratios in the notochord at tailbud stages 17–22. Inset shows F-actin localization in the notochord at tailbud stages 18 and 22. (F) Quantification of ventral-to-dorsal pS19-MRLC intensity ratios in the notochord at tailbud stages 17–22. Inset shows myosin localization of the notochord at tailbud stages 18 and 22. Data are mean \pm s.d. Red dashed line shows ratio=1. Scale bars: 100 μ m.

Asymmetrical actomyosin constriction in the notochord is required for *Ciona* embryonic tail bending

To determine whether embryonic tail bending requires actomyosin contractility, we inhibited actomyosin activity during early (tailbud stages 16 and 17) and later (tailbud stage 21) embryonic tail bending stages using chemical inhibitors Y-27632 and blebbistatin, respectively. We observed embryonic tail-bending defects in all treatment groups, with more severe tail-bending abnormality at early tailbud stages (tailbud stages 16 and 17) (Fig. S2). To determine whether contractility is the driving force behind notochord bending, we performed genetic manipulation experiments to disrupt the actomyosin apparatus, specifically in the notochord. Previous studies in *Ciona* and *Drosophila* have reported that introducing an unphosphorylatable form of MRLC (T18A-S19A) decreases myosin activity and alters tissue morphogenesis (Denker et al., 2015; Kasza et al., 2014). Therefore, we overexpressed the nonphosphorylatable MRLC mutant (T18A-S19A) in the notochord. The T18A-S19A-expressing notochord showed less tail-bending morphology ($n=47/72$; Fig. 3A, bottom) compared with the control group (Fig. 3A, top). Quantitative data showed that θ in the T18A-S19A-expressing embryos was $39.9^\circ \pm 19^\circ$ (mean \pm s.d., $n=47$; Fig. 3B), significantly lower compared with the control group ($\theta=75.4^\circ \pm 17^\circ$, $n=20$; Fig. 3B).

Cofilin, a highly conserved actin-binding protein, plays an important role in many cellular processes (Lappalainen and Drubin, 1997), such as the furrow formation in cytokinesis (Abe et al., 1996; Nakano and Mabuchi, 2006) and cell elongation in *Ciona* notochord morphogenesis (Sehring et al., 2014). In mammals, cofilin phosphorylation at serine 3 prevents cofilin-actin binding and stabilizes F-actin. Overexpression of

the nonphosphorylatable cofilin mutant cofilin S3A inhibits RhoA-stimulated actin polymerization (Arber et al., 1998; Sotiropoulos et al., 1999). *Ciona* has only one cofilin gene, in which serine 5 is equivalent to the serine 3 in mammalian cofilin (Sehring et al., 2014). To disrupt F-actin dynamics, we made *Ciona* cofilin S5A mimic the nonphosphorylated cofilin acting as a dominant-negative cofilin mutant and electroporated it into *Ciona* embryos. The results showed that the difference between ventral and dorsal F-actin enrichment was greatly reduced in the cofilin S5A-expressing notochord ($n=16/24$; Fig. 3C, bottom) compared with the control group ($n=15/19$; Fig. 3C, top). Quantitative data showed that θ in the cofilin S5A group was $52.03^\circ \pm 17.9^\circ$ ($n=43$; Fig. 3D), which was lower compared with the control group ($\theta=80.20^\circ \pm 19.77^\circ$, $n=21$; Fig. 3D). Thus, disruption of both myosin II and F-actin activities and localization data showed that asymmetrical actomyosin contractility along the ventral side of the notochord is required for embryonic tail bending.

Differential epidermis proliferation is required for embryonic tail bending

Next, we measured the tail epithelial cell geometry and counted the number of cells at the dorsal and ventral sides of the notochord, respectively. Although the cell geometry was different (Fig. S3A-E), the more prominent phenotype was the number of cells (Table S1). BrdU staining of *Ciona* embryos showed that the dorsal region, including the dorsal midline of the tail epidermis and neural tube, contained more dividing cells compared with the ventral region, including the ventral midline of the tail epidermis and endodermal strand (Fig. 4A-C; Movie 5). The number of divided dorsal epithelial

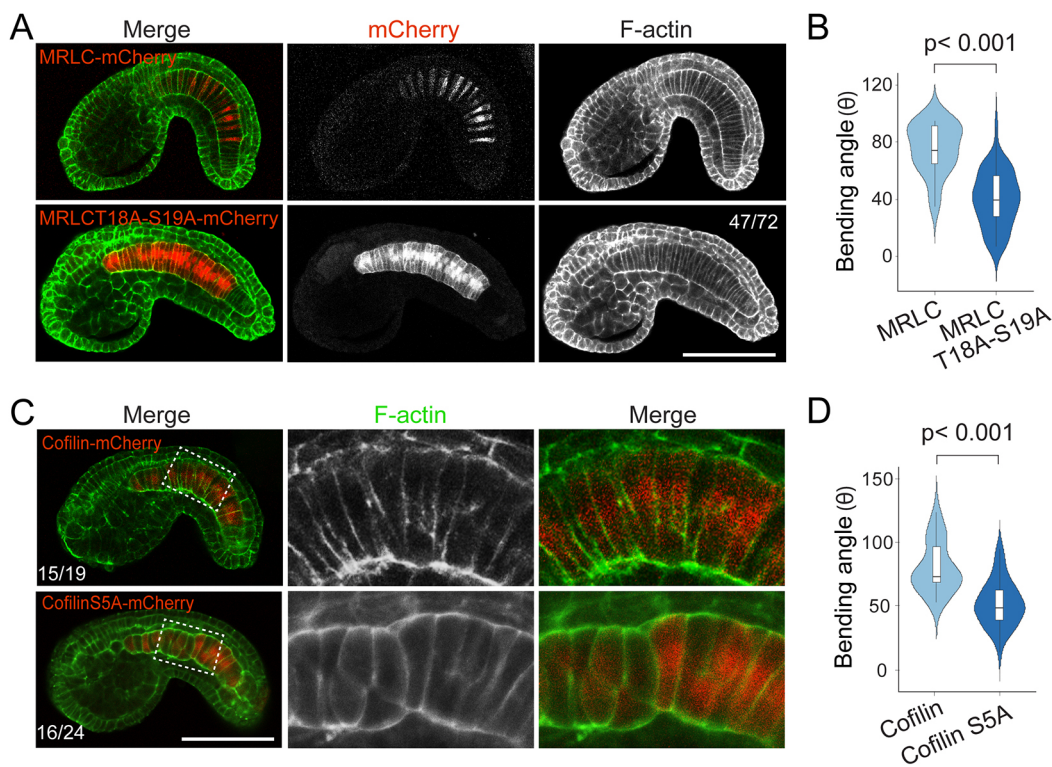


Fig. 3. Actomyosin contractility is required for notochord and embryonic tail bending in *Ciona robusta*. (A) Embryonic tail bending is disrupted in MRLC-T18A-S19A-mCherry-expressing *C. robusta* embryos ($n=47/72$) (bottom) compared with MRLC-mCherry-expressing embryos (top). The embryo morphology is shown by Phalloidin staining (tailbud stage 21). (B) Quantification of the bending angle θ of MRLC-mCherry-electroporated ($n=20$) and MRLC-T18A-S19A-mCherry-electroporated ($n=47$) embryos. (C) Confocal images (median sections) showing morphologies of cofilin-mCherry-expressing (top) and cofilinS5A-mCherry-expressing (bottom) embryos (tailbud stage 20). The embryos were stained with Phalloidin to show F-actin. Panels on right show higher-magnification images of the boxed area. (D) Quantification of the bending angle θ of cofilin-mCherry-expressing ($n=21$) and cofilinS5A-mCherry-expressing ($n=43$) embryos. Violin plots show the distribution of bending angles θ ; median (horizontal line), interquartile range (box), s.d. (whiskers) and density plot of frequency. Scale bars: 100 μ m.

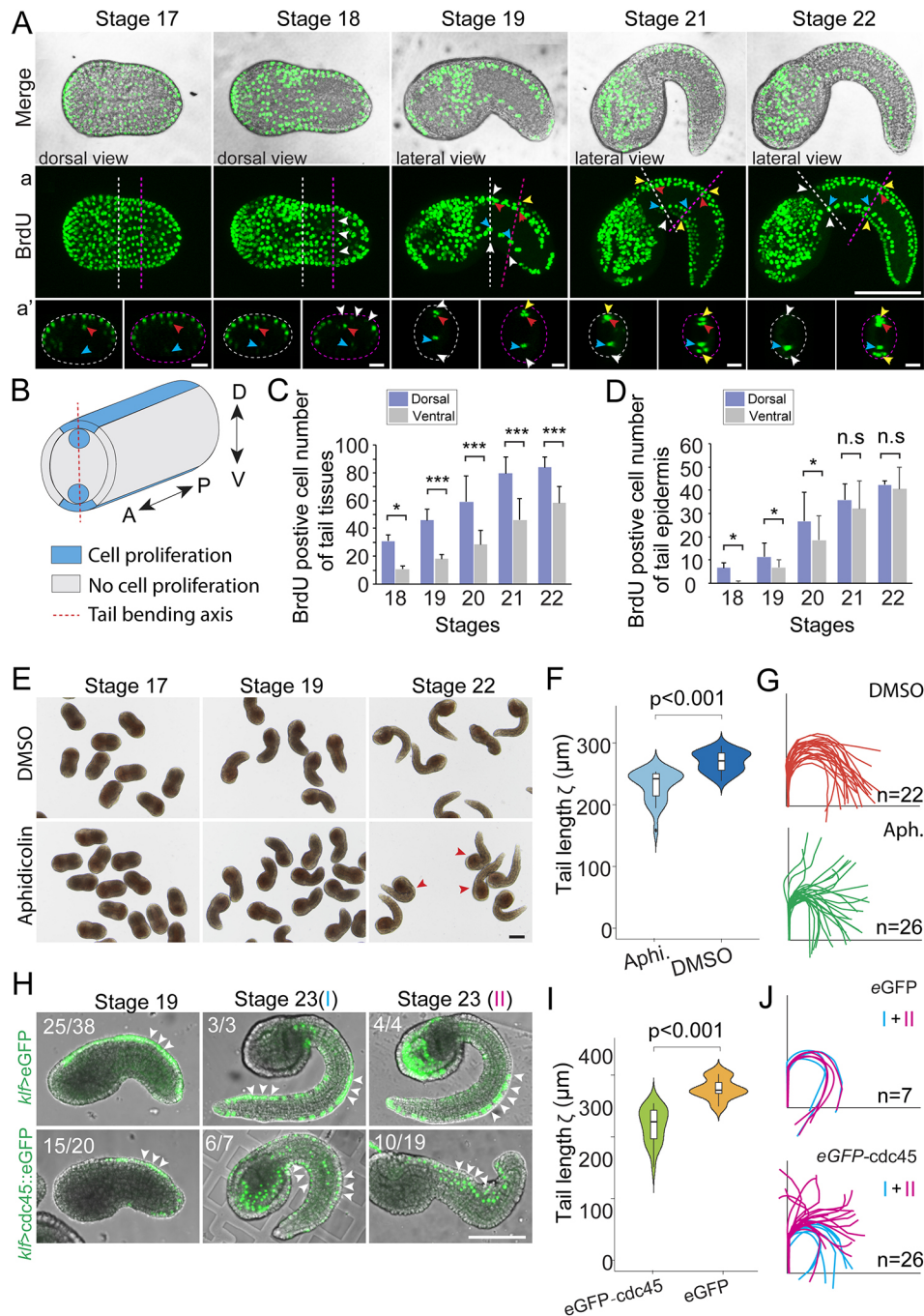


Fig. 4. Differential epidermis proliferation is required for embryonic tail bending in *Ciona robusta*. (A) Confocal images (projection) showing distribution of BrdU-positive cells in embryos at tailbud stages 17–22. BrdU-positive cells (green) merged with the differential interference contrast (DIC) image of the same embryo (top). BrdU-positive cells in the neural tube (red arrowheads), endodermal strand (blue arrowheads) and epidermis (yellow arrowheads) and BrdU-negative cells in the epidermis (white arrowheads) (a). Views from the axial plane of the tail at anterior (white dashed line) and middle (magenta dashed line) part of embryos (a'). (B) Model explaining the cell proliferation pattern in the tail on the basis of BrdU staining results. Cell proliferation in the dorsal domain of the tail involves the dorsal midline of the tail epidermis and neural tube, whereas the ventral domain includes the ventral midline of the tail epidermis and endodermal strand. (C) Quantification of BrdU-positive cell number in dorsal and ventral domains of the tail epidermis at tailbud stages 18–22. (D) Quantification of BrdU-positive cell number in dorsal and ventral domains of the tail epidermis at tailbud stages 18–22. (E) DIC images displaying morphologies of DMSO-treated (top) and aphidicolin-treated (bottom) embryos at tailbud stages 17, 19 and 22. DMSO and aphidicolin treatment was started at tailbud stage 16. (F) Quantification of tail length ζ of DMSO-treated ($n=24$) and aphidicolin-treated ($n=24$) embryos at tailbud stage 22. (G) Shape of DMSO-treated ($n=22$) and aphidicolin-treated ($n=26$) tailbud embryos at stage 22. The embryo shape is produced by plotting the axial line of the embryo; the anterior end of the axial line is located at (0, 0) Cartesian coordinates. Each line represents one individual embryo. (H) Confocal images (projection) showing morphologies of *klf>eGFP*-transfected (top) and *klf>eGFP::cdc45*-transfected (bottom) embryos (tailbud stage 19 or 23). White arrowheads show the locations in which the transgene is expressing dominantly. (I) Quantification of tail length ζ of *klf>eGFP*-transfected ($n=8$) and *klf>eGFP::cdc45*-transfected ($n=25$) embryos at tailbud stage 23. (J) Shapes of *klf>eGFP*-transfected (top) and *klf>eGFP::cdc45*-transfected (bottom) embryos at tailbud stage 23. Embryo shapes were determined as described in G. The collective magenta and blue lines represent the embryo shape of gene expression patterns of I and II, shown in H, respectively. Data (C,D) are mean \pm s.d. * $P < 0.05$, *** $P < 0.001$ (two-tailed Student's *t*-test). n.s., not significant. Violin plots (F,I) show the distribution of tail length ζ ; median (horizontal line), interquartile range (box), s.d. (whiskers) and density plot of frequency. Scale bars: 100 μm (A,E,H).

cells was significantly higher compared with the ventral epithelial cells (Fig. 4D).

To determine the role of differential epidermis proliferation activity in embryonic tail bending, we blocked cell proliferation by incubating embryos at tailbud stage 16 using the DNA replication inhibitor aphidicolin (Ikegami et al., 1978). BrdU staining confirmed the efficiency of cell cycle inhibition by aphidicolin (Fig. S3H). Embryos developed normally, at least without detectable abnormality during the early tailbud stages (tailbud stages 17–19) in the aphidicolin-treated group (Fig. S3F,G). However, embryos showed abnormal morphology with a shorter and ill-bent tail at tailbud stage 22 (Fig. 4E–G; Fig. S3F), indicating that cell proliferation plays an essential role in embryonic tail bending at later tailbud stages.

To further analyze the contribution of differential epidermis proliferation dorsally and ventrally, we used the mosaic expression pattern of electroporated transgenes in *Ciona* embryos (Zeller et al., 2006). Ectopic *Ci-cdc45* overexpression inhibited epithelial cell proliferation (Fig. S3I), although the underlying mechanism was unclear. *Ci-cdc45* was ectopically overexpressed under the control of the *klf1/2/4* promotor, exclusively expressed in the dorsal and ventral midline of the epidermis of *Ciona* embryos (Pasini et al., 2006). We found that the epithelial cell proliferation inhibited by *Ci-cdc45* overexpression leads to shorter tail length compared with the control embryo at tailbud stage 23 (Fig. 4H,I), mimicking the effect of aphidicolin treatment (Fig. 4E,F). Tail bending was normal at the early tailbud stage (tailbud stage 19) (Fig. 4H), but we found two distinct phenotypes because of two different expression patterns of the transgene at a later tailbud stage. Tail bending was normal when *Ci-cdc45* was expressed symmetrically in the dorsal and ventral midline of the epidermis [Fig. 4H,J, pattern I (blue)]. In contrast, when *Ci-cdc45* was dominantly expressed in the dorsal midline of the epidermis, the embryonic tail bent dorsally and presented a more diverse morphology [Fig. 4H,J, pattern II (pink)].

Together, our findings show that both asymmetrical actomyosin constriction of the notochord and differential epidermis proliferation are required for embryonic tail bending in *Ciona*.

Dominant role of asymmetrical actomyosin constriction in embryonic tail bending

The above results show that both asymmetrical actomyosin constriction of the notochord and differential cell division in the epidermis are required for the embryonic tail bending in *C. robusta*, but we are yet to determine the main driving force in this event. From a mechanics perspective, both of them can drive tail bending, as long as the induced force is large enough. We measured the Young's moduli, the parameter that describes material stiffness, of the notochord, muscle and epidermis by nanoindentation using an atomic force microscope (AFM) (Fig. 5A,B). Measurements showed that the Young's moduli of the notochord, muscle and epidermis decrease in turn (Fig. 5C). It is more likely that the main driving force of embryonic tail bending originates from the bending of the notochord, the stiffest tissue, than the asymmetrical division of the relatively soft epidermal cells. To verify our hypothesis, a finite element model was built using Abaqus (Hibbitt et al., 2011), as shown in Fig. 5D.

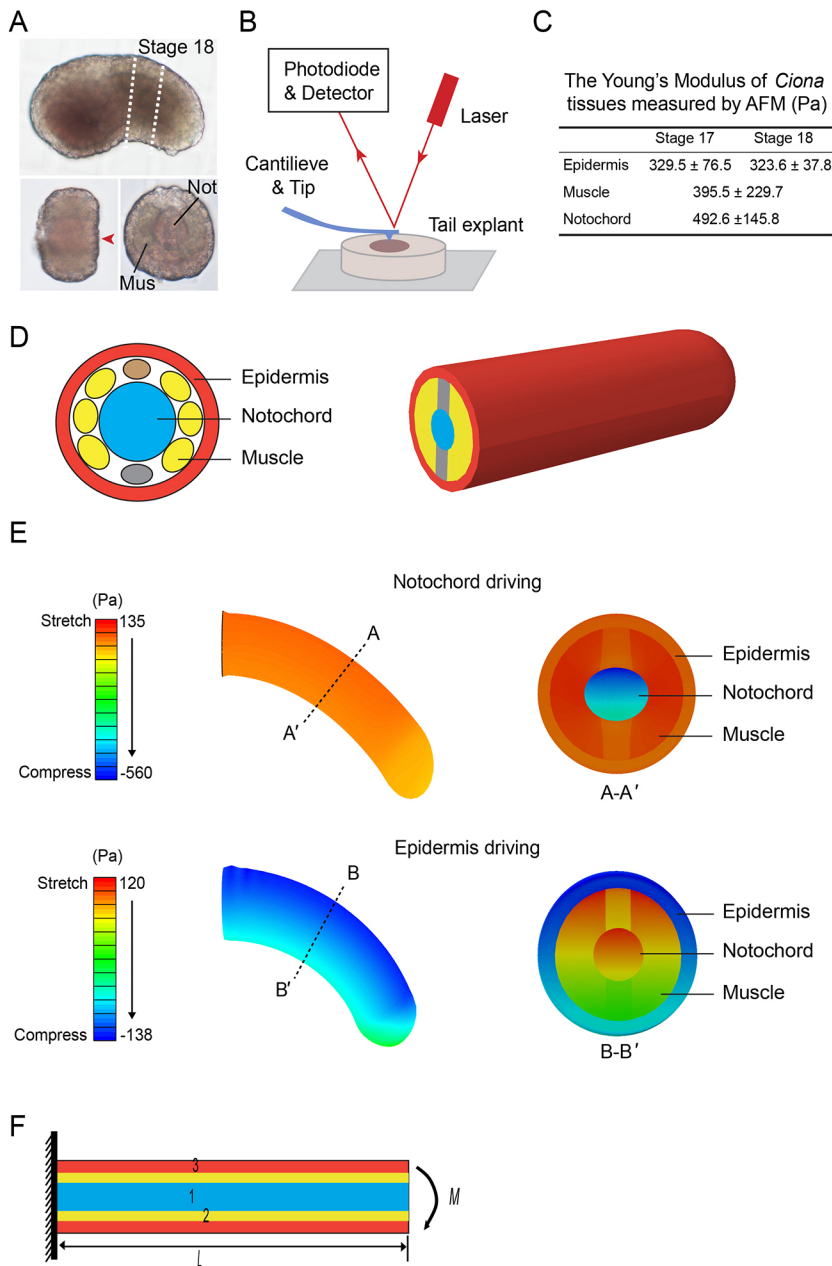
In the finite element simulations, we considered two extreme situations: the contraction of the notochord serves as the exclusive driving force, and the differential cell division serves as the exclusive driving force. The contraction of the notochord and the cell division are treated by including a growth field. The enlargement of the tissues arising from cell elongation and division can be simulated by introducing a positive growth ratio. The contraction of the tissues, by

contrast, can be achieved by introducing a negative growth ratio. To simulate the bending of the tail, a simple and typical method is to include a gradient growth field (Fig. S4A). For the notochord-driving scenario, the elongation and contraction of the notochord are considered together and included by a gradient growth field, whereas the epidermal cells are treated as a passive material, undergoing elastic deformation. For the differential cell division-driving scenario, the differential cell division is included by a gradient growth field, whereas the notochord is treated as a passive material. In the simulation, we can adjust the magnitude of the growth field to fit the bending angle and the elongation of the tail observed in the experiments. However, the stress or strain level in the tail does not influence the relative contributions of the epidermis and notochord. The results show that, if the contraction of the notochord serves as the main driving force for tail bending, the epidermis should be stretched along the AP axis (Fig. 5E, top). On the contrary, if the differential cell division drives the tail bending, the epidermal cells at the ventral side should be squeezed (Fig. 5E, bottom). To test which scenario is correct, we measured the epidermal cell geometry and found that the dorsal and ventral epidermal cells flattened gradually in the DV direction as the tail bends (Table S1). Owing to the Poisson's effect, a material tends to expand in the directions perpendicular to the direction under compression. Conversely, if the material is stretched, it usually tends to shrink in the perpendicular directions. Therefore, the flattening of the epidermis on both dorsal and ventral sides suggests that the epidermal cells are stretched along the AP axis. It is worth noting that elongation of the notochord is neglected in the exclusive epidermis-driving scenario. The elongation of the notochord will stretch the epidermal cells and counteract the compression of the epidermal cells to some extent. Thus, we cannot totally exclude the possibility that cell division plays a role in tail bending. In this vein, the differential cell division may drive the tail bending, only up to a point. To quantify the contributions of the notochord and epidermis, we further propose a theoretical physical model (see Supplementary Materials and Methods). Based on geometric parameters of the same embryo for different stages (Table S1), we calculated the contributions of the epidermis differential cell division and the notochord contraction. The results show that the bending moment induced by the epidermis is dispensable compared with the moment required to bend the tail (Fig. S4). Therefore, the contribution of differential cell division in the epidermis to the tail bending is relatively limited at the initial stage.

To evaluate whether the ventral constriction of the notochord is sufficient to drive tail bending, we theoretically treated the tail as a cylindrical beam consisting of three layers representing the notochord, muscle and epidermis, respectively (Fig. 5F). Bending stiffness was used to evaluate the resistance of the beam to bending. According to the Euler-Bernoulli beam theory, the bending stiffness of the tail is expressed as:

$$EI_z = \frac{E_n \pi d_1^4}{64} + \frac{E_m \pi d_2^4}{64} \left(1 - \frac{d_1^4}{d_2^4}\right) + \frac{E_e \pi d_3^4}{64} \left(1 - \frac{d_2^4}{d_3^4}\right), \quad (1)$$

where E_n , E_m and E_e are the Young's moduli of the notochord, muscle and epidermis, respectively; d_1 , d_2 and d_3 are diameters of the notochord, muscle and epidermis, respectively; and I_z is the moment of inertia of the beam's cross-section. According to Eqn 1, the tail's resistance to bending depends on the geometry and mechanical properties of the embryo. We quantified the bending angle using the proposed biomechanical model when the constriction of notochord is the driving force. At the initial stage of tail bending, the notochord actomyosin contracts actively at the ventral side, and produces a



bending moment on the beam. The bending moment, M , produced by the contraction force f_c is:

$$M = \frac{f_c d_1}{2}. \quad (2)$$

The rotational angle α at the free end of the beam can be calculated by:

$$\alpha = \frac{ML}{EI_z}, \quad (3)$$

where L is the length of the tail. It can be seen from Eqns 1-3 that the rotational angle correlates negatively with the diameter of notochord when the contraction force is conserved. Therefore, less contraction force is required to bend the tail as the tail elongates. According to our experiments, the tail elongates and bends simultaneously. Therefore, the force needed to bend the tail decreases as the tail elongates. Our experiments showed that the accumulation of actin and myosin at the ventral side of the notochord weakens as the tail bends, further supporting the above theoretical prediction.

Fig. 5. Biomechanical model for calculating forces and deformations in embryonic tail bending. (A) Images showing how the tail explant is cut from the embryo at tailbud stage 18. Embryos were cut transversely, and nanoindentations were performed on cross-sections.

(B) Young's modulus measurement using an AFM equipped with a cantilever with a sharp tip (probe) at its end, which is used to scan the specimen surface. The cantilever is typically silicon or silicon nitride, with a tip radius of curvature in the order of nanometers. When the tip is brought into the proximity of a sample surface, forces between tip and sample lead to cantilever deflection, which can be measured using a laser unit and photodiode detector.

(C) Table showing the Young's modulus of *C. robusta* using an AFM. (D) Finite element model consisting of three layers. The tail geometry is theoretically treated as a combination of cylinder and hemisphere. The mechanical properties of notochord and epidermis from C are used: notochord 500 Pa, epidermis 300 Pa. The contraction and division of cells are simulated by exerting a thermal field in the model.

(E) Images showing representative results of different driving mechanisms, in which color encodes stress (Pa) on each point. If the asymmetrical actomyosin constriction of notochord is the main cause of tail bending, the epidermis will be in a tensile stress state (top). On the contrary, if the differential cell proliferation is the main driving force, the epidermis will be in a compressive stress state (bottom).

(F) A simplified composite beam model accounting for the mechanical mechanism of tail bending. The tail is simplified as a multilayer cylinder beam, representing the combined effects of epidermis, muscle and notochord, respectively. The restriction of the head is treated as fixed constraint. The contraction force of the notochord is equivalent as a moment at the free end.

Owing to the difficulty of experimental measurement of constriction force in the notochord *in vivo*, we took the value of the constriction force in actin bundles of cell groups for reference: f_c is in the order of 10 nN (Effler et al., 2006; Poirier et al., 2012; Soiné et al., 2015; Zhang and Robinson, 2005). Though the reference value may deviate from the actual value of *Ciona*, this does not affect the underlying mechanical mechanisms. The rotational angle α was calculated to be $\sim 24.2^\circ$ when $f_c = 20$ nN, which is equal to the tail bending angle θ (Fig. S5). This result suggests that actomyosin constriction at the ventral side of the notochord is sufficient to drive the embryonic tail bending in *C. robusta*.

DISCUSSION

In *Ciona* embryogenesis, the embryonic tail bends and elongates smoothly and continually. In this study, we presented data to show that *Ciona* embryonic tail bending is an autonomous large-scale morphogenic process mediated by tail tissues and controlled by genetics. During the early tailbud stage, the notochord generates

asymmetrical contractile forces to drive embryonic tail bending, whereas differential epidermis proliferation dorsally and ventrally plays a permissive role and allows embryonic tail bending (Fig. 6). These results show a robust tail-bending mechanism at the embryonic scale and deepen our understanding of embryonic tail bending commonly found in invertebrates and vertebrates.

The notochord, typically found in chordate embryos, is located in the midline of the embryonic tail. It acts as a signaling center and provides structural support (Stemple, 2005). A mechanical challenge for the *Ciona* embryo to overcome during embryonic tail bending is mechanical resistance produced by the stiff notochord. Our analysis of the actomyosin network in *Ciona* embryos during early tail bending showed asymmetrical accumulation of actomyosin at the ventral side of the notochord, which generates mechanical forces to drive tail bending by contractility that is orthogonal to the bending axis. Polarized actomyosin contractility, such as apical or basal constriction, plays an essential mechanical role in tissue bending and/or folding (Gutzman et al., 2008; Haigo et al., 2003; Lee and Goldstein, 2003; Martin et al., 2009; Nicolás-Pérez et al., 2016; Nishimura et al., 2012; Sherrard et al., 2010). The notochord, and hence embryonic tail bending, show defects as actomyosin organization and activities decrease because of myosin II and cofilin mutations. Our physical model predicted that the polarized actomyosin contractility along the ventral side of the notochord is sufficient to drive embryonic tail bending. Therefore, the notochord is the key driver of tail bending in *Ciona* embryogenesis.

Polarized actomyosin localization has been found in the *Ciona* notochord and plays an indispensable role in notochord morphogenesis. For example, the tip polarization of actin is important for notochord convergence/extension (CE) (Munro and Odell, 2002), whereas anterior polarization of myosin and the contractile ring are important for notochord elongation (Newman-

Smith et al., 2015; Sehring et al., 2014). The actomyosin in the notochord displays clear DV polarity patterning during the early tailbud stage, which is required for embryonic tail bending. How the actomyosin is directed to accumulate along the ventral side of the notochord at the early tailbud stage is unclear. Some proteins, such as those found in the extracellular matrix, also show polarity during notochord morphogenesis (Oda-Ishii et al., 2010; Veeman et al., 2008). Interestingly, during notochord CE, the notochord preferentially accumulates basement membrane marker laminin dorsally and the apical cell polarity molecule atypical protein kinase C (aPKC) ventrally (Oda-Ishii et al., 2010), which might provide a polarizing cue for polarized actomyosin enrichment.

We also provided evidence of an epidermis-dependent mechanism regulating tail bending at later tailbud stages. BrdU staining showed that dorsal midline cells in the tail epidermis divide faster compared with the ventral side during embryonic tail bending. Spatial differences in cell proliferation rates can cause folding and/or bending shapes during development (Mao et al., 2013; Miller et al., 1999; Tozluoglu et al., 2019). However, our results revealed that this bias in cell proliferation is required for embryonic tail bending at late tailbud stage rather than early tailbud stage. It appears that the tail epidermis plays a dominant role in producing the tail-bending structure at late tailbud stage. Consistent with this, tail-bending deficiencies were observed at late tailbud stage of miniature (dwarf) tailbud embryos, which are composed of relatively smaller epidermal cells compared with wild-type embryos, indicating that overall decrease in the number of epidermal cells changes the mechanical state of the tailbud embryos (Matsumura et al., 2020). In this study, we believe that the faster cell proliferation in the dorsal midline epidermis can release the accumulated mechanical stress generated by asymmetrical notochord contractility and/or promotes polarized tissue shrinkage of tail epidermis. Both mechanisms are able to facilitate embryonic tail bending ventrally, which is confirmed by the fact that cell proliferation inversion at the dorsal midline of the tail epidermis causes embryonic tail bending dorsally at later tailbud states. In addition, tail epidermal cells tend to divide parallel to the AP axis during the early tailbud stages (Negishi et al., 2016; Ogura et al., 2011), which supports the idea that this oriented cell proliferation might also participate in the relief of local tissue resistance along the AP axis, facilitating embryonic tail bending. Mechanical stretching promotes epithelial cell proliferation (Gudipaty et al., 2017). Therefore, it would be interesting to analyze whether mechanochemical feedback exists between mechanical stretching and differential epidermis proliferation (speed and/or orientation) in *Ciona* embryonic tail bending.

The notochord and tail epidermis are both essential for *Ciona* embryonic tail bending. However, tail bending likely originates from the overall effect of the high coordination between different tail tissues. Indeed, the polarized contractility of the notochord plays a major role in shaping the bending tail at early tailbud stages, whereas bias of differential epidermal proliferation ensures the robustness of tail bending at later tailbud stages. However, our data did not rule out the possibility that other tissues and their interactions also contribute to embryonic tail bending. For example, embryos treated with SU5402, the fibroblast growth factor signaling inhibitor, showed morphologically defective tail bending and elongation, although the notochord preserved its bending property (Ikuta et al., 2010), indicating that the role of the notochord in driving embryonic tail bending depends on the synergistic effect of other tissues. In addition, a posterior-to-anterior zipper event occurs during the same period as early embryonic tail bending in the neural tube (Hashimoto et al., 2015), which

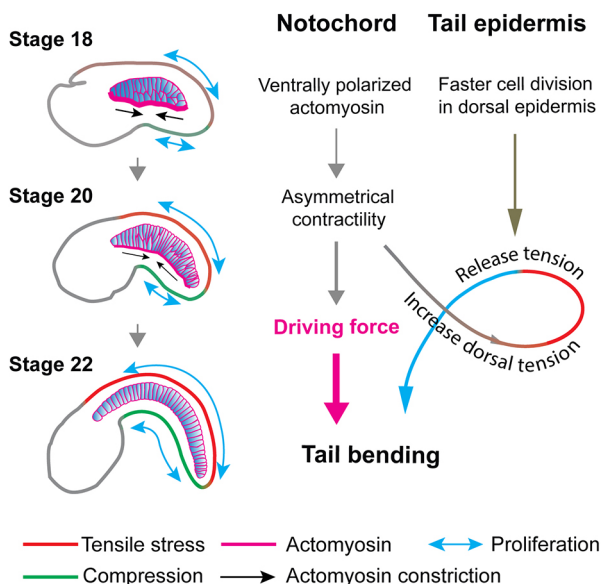


Fig. 6. Model of embryonic tail bending in *Ciona robusta*. During *C. robusta* embryonic development, the embryo tail bends ventrally, which coincides with the appearance of asymmetrical actomyosin along the ventral side of the notochord. This polarized contractile actomyosin network drives the notochord and, hence, embryonic tail bending ventrally. A predicted dorsal tension accumulates as the tail bends continuously, which can hamper embryonic tail bending. To avoid rupture, this tension is dissipated by faster differential epidermis proliferation in the dorsal tail. Therefore, the notochord and epidermis coordinate to drive embryonic tail bending in *C. robusta*.

asymmetrically localizes on the dorsal side of the embryos. Whether this cellular process affects embryonic tail bending is unclear.

According to von Baer's laws (von Baer, 1928), vertebrate embryos converge on a common physical structure and hence show a similar morphology during early embryogenesis, called phylotypic stages (Hall, 1997). For example, at the beginning of neurulation, the embryo in chordates is commonly C-shaped (Gilbert and Barresi, 2016). Embryonic tail bending helps embryos elongate continuously within the chorion without mechanical damage. In tunicates, the closest living relatives of vertebrates (Delsuc et al., 2006), the embryos also show a bending morphology at a similar tailbud stage. This interesting phenomenon gives rise to the question, why and how do embryos assume a bending shape from the viewpoint of evolution and development? Our study of the mechanism of ascidian embryonic bending is a first step toward our understanding of embryo bending in an evolutionary perspective.

Conclusions

Embryonic tail bending within the chorion is a chorion-independent process under genetic control. The head and trunk are not required for tail bending, suggesting that it is a self-organized event. Furthermore, we showed the existence of ventrally localized actomyosin in the notochord and differential epidermis proliferation between the dorsal and ventral midline during embryonic tail bending. Through a combination of genetic perturbation and chemical drug manipulation, we revealed that both asymmetrical notochord contractility and differential epidermis proliferation are important for embryonic tail bending. Asymmetrical notochord contractility is sufficient to drive embryonic tail bending, whereas differential epidermis proliferation is a passive response to mechanical forces. Our findings provide insights into how different tissues coherently coordinate to achieve a large-scale morphogenetic event at the embryonic level. The mechanisms underlying embryonic tail bending in structure-simple chordate embryos will help us understand their more complex counterparts in vertebrate systems.

MATERIALS AND METHODS

Experimental model

Adult *C. robusta* individuals were collected from the Yellow Sea in Weihai, China and kept in a recirculating aquarium at 18°C until analysis.

Embryo culture and manipulation

All procedures involving live animals were performed in filter-fresh seawater. Developing embryos were staged according to the criteria provided by Hotta et al. (2007).

Fertilized eggs were dechorionated, as previously described (Corbo et al., 1997). The fertilized eggs (10 min post fertilization) were immersed in seawater containing 1% sodium thioglycolate, 0.05% protease E and 32 µl of 10 N NaOH. The chorion was removed within 5 min at room temperature (RT) by gently pipetting. Dechorionated eggs were washed four times with filter-fresh seawater and transferred into 1% agarose-coated plastic Petri dishes for culturing or immediately used for plasmid electroporation. Embryos were cultured at 16°C.

For tail-cut experiments, embryos at tailbud stage 19 were used, unless otherwise specified. All procedures were performed in a room maintained at ~20°C. A hand-held glass needle was prepared by pulling a glass capillary. Each embryo was carefully cut along the boundary between trunk and tail to obtain isolated tail fragments (CT). The A-CT or P-CT was obtained by further cutting CT fragments.

Plasmid DNA (60 µg or 80 µg in 80 µl) was mixed with 420 µl of 0.77 M mannitol in 4 mm cuvettes. Then 300 µl of dechorionated fertilized eggs was added and electroporated. Electroporated embryos were cultured in Millipore-filtered seawater at 16°C or 18°C.

Plasmid constructs

A *C. robusta* *klf 1/2/4* promoter was PCR-amplified by the forward primer 5'-CTCAAGCTTCGAATTCGGCATATGATACATCATGTGTGTCT-3' and reverse primer 5'-GGCGACCGGTGGATCCTTCAAACCAATTAC-CATTTCGTCTA-3'. The purified PCR product was inserted into promoter-less enhanced green fluorescence protein 1 (pEGFP-1) to create *klf>eGFP* using the standard In-Fusion® cloning protocol (TaKaRa Bio). *Cr-cdc45* was amplified using the primer obtained from Sehring et al. (2014). The eGFP::*Cr-cdc45* was obtained from cytomegalovirus (CMV)>eGFP::*Cr-cdc45* digested with BamHI and NotI. The eGFP complementary DNA (cDNA) of *klf>eGFP* was replaced by a cDNA of eGFP::*Cr-cdc45* to create *klf>eGFP::cdc45*. *Cr-cofilin S5A* was PCR-amplified by the forward primer 5'-ATGGGCGTAAGTGCCGGAATTA-3' and the reverse primer 5'-TT-AGACATATTCATATGCGTTACT-3'. The PCR products were used to create entry clones using the pCR8/GW/TOPO system (Invitrogen). The entry clone was used to generate cofilinS5A-mCherry expression constructs using the destination vector Minos-B3-eBra-bpFOG-B5::R1-ccdB/CmR-R2-mCherry (Dong et al., 2009). The following expression constructs have been described previously: MRLC-mCherry (Dong et al., 2011), MRLC T18A-S19A-mCherry (Denker et al., 2015) and cofilin-mCherry (Sehring et al., 2014).

Time-lapse imaging

Time-lapse movies were taken using either a Nikon Eclipse Ni fluorescence or a Nikon A1 confocal microscope. To observe the development of chorionated and dechorionated tailbud embryos, or cut tails (CT, A-CT and P-CT), corresponding embryos or isolated tails were captured under a microscope equipped with a DS-Ri2 camera, the interval between frames was 30 s. The duration depended on embryo development at ~20°C and was ~2 h for all CT developments.

Drug treatment

To inhibit cell proliferation, embryos were treated with 2 µg/ml aphidicolin or dimethyl sulfoxide (DMSO; control) at the start of the tailbud stage. All embryos were cultured and imaged at ~20°C. Imaging was performed using the Eclipse Ts2R inverted microscope (Nikon), and images of developing embryos were captured manually every 30 min until 3.5 h post-treatment. To inhibit actomyosin activity, embryos at 8 h post fertilization (hpf), 9 hpf and 11 hpf at 18°C were treated with 100 µM blebbistatin or 200 µM Y-27632 and imaged subsequently in a room maintained at 20°C.

Immunostaining and quantification

Embryos at tailbud stages 17-22 were collected and fixed with 4% paraformaldehyde (PFA) in seawater for 2 h at RT. The fixed embryos were washed thrice with phosphate-buffered saline (PBS) containing 0.1% Triton X-100 (PBST) for 15 min each time. To detect F-actin, the fixed embryos were stained with 1/200 Alexa Fluor® 488-conjugated Phalloidin (Invitrogen, 11791-020) in PBS overnight at 4°C. They were washed thrice with PBS, mounted using Vectashield (Vector Laboratories) mounting medium with 4',6-diamidino-2-phenylindole (DAPI), and stored at 4°C.

For pS19 MRLC staining, we followed the procedure as described previously by Sherrard et al. (2010) with minor modifications. Embryos at tailbud stage 17-22 were collected and fixed in 100 mM 4-(2-hydroxyethyl)-1-piperazineethanesulfonic acid (HEPES; pH 6.9-7.0), 100 mM ethylene glycol-bis(β-aminoethyl ether)-N,N,N',N'-tetraacetic acid (EGTA; pH 7.0), 10 mM MgSO₄, 2% formaldehyde, 0.1% glutaraldehyde and 300 mM dextrose for 1 h. Next, the embryos were washed thrice with PBST and then thrice with PBS. To reduce unreacted aldehydes, the embryos were treated with 0.1% sodium borohydride in PBS for 20 min and then washed thrice with PBS. Fixed embryos were blocked using 0.1% bovine serum albumin in PBS for 1 h at RT and then incubated with ser19 phospho-myosin (1/250; Cell Signaling Technology, 3671) for 48 h at RT. Next, they were washed thrice within 8 h and incubated with Alexa Fluor® 568-conjugated anti-rabbit immunoglobulin G (IgG) secondary antibody (1/250; Invitrogen, A11011) for 48 h at RT. Finally, the embryos were rinsed thrice and then mounted for imaging, as described above.

To detect cell proliferation, we used the standard procedures for BrdU staining, as described previously (Sehring et al., 2014). Embryos were treated with BrdU (Invitrogen, B23151) at 8.3, 9, 10, 11 and 12 hpf for 45 min at 18°C. The BrdU-incorporated embryos were washed twice with seawater for 10 min each time at 18°C and quickly fixed with 4% formaldehyde in seawater for 2 h at RT. To detect BrdU, the embryos were washed thrice with PBST, permeabilized in acetone for 10 min at −20°C and again washed thrice with PBST. Before immunostaining, the embryos were incubated in 4 N HCl for 10 min at RT to denature DNA, washed thrice, blocked with PBST containing 10% goat serum for 1 h at RT, and incubated with mouse anti-BrdU primary antibody (1/150; Invitrogen, B35128) for 16 h at 4°C. Next, the embryos were again washed thrice, incubated with Alexa Fluor® 568-conjugated anti-mouse IgG (1/300; Invitrogen, A21202) overnight at 4°C, rinsed thrice and finally mounted for imaging, as described above.

To thoroughly detect the F-actin distribution of the notochord, embryos positioned on the longitudinal, axial and coronal planes of the notochord were selected for imaging (Fig. 2; Fig. S2). The embryos were imaged using an A1 confocal microscope (Nikon). To measure relative fluorescence intensities (F-actin or pS19 MRLC) along the dorsal or ventral notochord edges, we obtained mean gray levels averaged over a line drawn along the notochord edges of interest using ImageJ (<https://imagej.nih.gov/ij/index.html>). For each measurement, we measured the maximum fluorescence intensity projections from the longitudinal view. To analyze the distribution of BrdU-positive cells, we rendered 3D projections of confocal images of BrdU-stained embryos in NIS-Elements AR ver. 4.40.00 (Nikon) and manually counted the number of BrdU-positive cells in the dorsal and ventral midline of the tail epidermis, neural tube and endodermal strand.

AFM measurement

To measure the Young's modulus of the notochord, muscle and epidermis, the embryo was cut transversely and then nanoindentation tests were conducted on cross-sections, as shown in Fig. 5A,B. An AFM (NT-MDT Spectrum Instruments) equipped with an IX71 optical microscope system (Olympus) was used (Kuznetsova et al., 2007). Nanoindentation was performed using an MLCT-O10 silicon nitride cantilever (200 µm long, 15 µm wide and 550 nm thick) with a spherical polystyrene tip (radius 5 µm) and a spring constant of 0.05 N/m (Bruker Corporation). Nanoindentation tests were repeated thrice at each selected position. Finally, the curves were fitted using the Hertz contact model (Hertz, 1881):

$$F = \frac{4ER^{0.5}}{3(1-\nu^2)}\delta^{1.5}, \quad (4)$$

where E and ν are the Young's modulus and Poisson's ratio of the indented tissue, respectively; R is the radius of the ball head on the cantilever beam, δ is the cell deformation distance and F is the force exerted on the cell. We took $\nu = 0.5$ unless stated otherwise. Several cells of the same kind were measured at a loading rate of 5 µm/s and an indentation depth of 300 µm. Cell stiffness was quantified using the averaged Young's modulus.

Finite element model

To further understand the mechanical mechanism underlying the tail bud bending, a three-dimensional finite element model was built (Fig. 5D). Its geometrical parameters were taken according to our experimental measurements (Table S1) and the Young's modulus of each component was taken from our AFM tests. The simulations were made using the software Abaqus (Dassault Systems). The system was meshed by C3D8R elements and a mesh sensitivity analysis was made to ensure that the element sizes did not interfere with the numerical results.

Quantitative analysis of embryonic tail bending

To quantify the tail length of an embryo, the length of the midline (Fig. 1B, green) of the tail was defined as tail length ζ . To quantify the embryonic tail-bending angle, we assigned the cross-angle of the magenta and blue lines (Fig. 1B) as the bending angle θ . The magenta line is along the boundary that separates tail and trunk territories, whereas the blue line intersects with the green line at the tail length.

Quantitative geometric analysis of embryos

To quantitatively analyze the embryo geometry, we labeled embryos using Phalloidin (Alexa Fluor® 488) at tailbud stages 17–22. Phalloidin staining helps to easily define cell boundaries of *C. robusta* embryos. We measured several aspects related to embryonic- or tissue-level geometries from the longitudinal view in median sections using ImageJ (<https://imagej.nih.gov/ij/index.html>) (Figs S1 and S3; Table S1).

Statistical analysis

All graphs in this study were produced using Matlab, Microsoft Excel or ggplot2 in R. The significance of differences was calculated using two-tailed Student's t -tests. $P < 0.05$ was considered statistically significant.

Acknowledgements

We thank lab members in the B.D. laboratory, Dr Prachi Richa from the University of Göttingen and Dr Xin Liang from Tsinghua University for the discussion and critical comments on the manuscript.

Competing interests

The authors declare no competing or financial interests.

Author contributions

Conceptualization: Q.L., Y.G., B.L., X.-Q.F., B.D.; Methodology: Q.L., Y.G., Y.F., H.P., W.S., B.L., Z.L., X.-Q.F., B.D.; Software: Y.G., B.L., X.-Q.F.; Validation: Q.L., Y.G., Y.F., H.P., W.S., B.L., Z.L., X.-Q.F., B.D.; Formal analysis: Q.L., Y.G., Y.F., H.P., W.S., B.L., Z.L., X.-Q.F., B.D.; Investigation: Q.L., Y.G., Y.F., H.P., W.S., B.L., Z.L., B.D.; Resources: B.D.; Data curation: W.S., Z.L., B.D.; Writing - original draft: Q.L., Y.G., B.L., X.-Q.F., B.D.; Writing - review & editing: Q.L., Y.G., H.P., W.S., B.L., Z.L., X.-Q.F., B.D.; Supervision: B.D.; Project administration: X.-Q.F., B.D.; Funding acquisition: X.-Q.F., B.D.

Funding

This work was supported by the Marine S&T Fund of Shandong Province for Pilot National Laboratory for Marine Science and Technology (Qingdao) (2018SDKJ0302-1), the National Natural Science Foundation of China (31572352, 31771649, 11921002 and 11620101001), the National Key Research and Development Program of China (2019YFE0190900), and the Taishan Scholar Project of Shandong Province, China (201502035).

Supplementary information

Supplementary information available online at <https://dev.biologists.org/lookup/doi/10.1242/dev.185868.supplemental>

Peer review history

The peer review history is available online at <https://dev.biologists.org/lookup/doi/10.1242/dev.185868.reviewer-comments.pdf>

References

- Abe, H., Obinata, T., Minamide, L. S. and Bamberg, J. R. (1996). Xenopus laevis actin-depolymerizing factor/cofilin: a phosphorylation-regulated protein essential for development. *J. Cell Biol.* **132**, 871–885. doi:10.1083/jcb.132.5.871
- Arber, S., Barbayannis, F. A., Hanser, H., Schneider, C., Stanyon, C. A., Bernard, O. and Caroni, P. (1998). Regulation of actin dynamics through phosphorylation of cofilin by LIM-kinase. *Nature* **393**, 805–809. doi:10.1038/31729
- Copp, A. J. and Greene, N. D. E. (2013). Neural tube defects—disorders of neurulation and related embryonic processes. *Wiley Interdiscip. Rev. Dev. Biol.* **2**, 213–227. doi:10.1002/wdev.71
- Corbo, J. C., Levine, M. and Zeller, R. W. (1997). Characterization of a notochord-specific enhancer from the Brachyury promoter region of the ascidian, *Ciona intestinalis*. *Development* **124**, 589–602.
- Delsuc, F., Brinkmann, H., Chourrout, D. and Philippe, H. (2006). Tunicates and not cephalochordates are the closest living relatives of vertebrates. *Nature* **439**, 965–968. doi:10.1038/nature04336
- Denker, E., Sehring, I. M., Dong, B., Audisio, J., Mathiesen, B. and Jiang, D. (2015). Regulation by a TGFβ-ROCK-actomyosin axis secures a non-linear lumen expansion that is essential for tubulogenesis. *Development* **142**, 1639–1650. doi:10.1242/dev.117150
- Di Gregorio, A., Harland, R. M., Levine, M. and Casey, E. S. (2002). Tail morphogenesis in the ascidian, *Ciona intestinalis*, requires cooperation between notochord and muscle. *Dev. Biol.* **244**, 385–395. doi:10.1006/dbio.2002.0582

- Dong, B., Horie, T., Denker, E., Kusakabe, T., Tsuda, M., Smith, W. C. and Jiang, D. (2009). Tube formation by complex cellular processes in *Ciona intestinalis* notochord. *Dev. Biol.* **330**, 237–249. doi:10.1016/j.ydbio.2009.03.015
- Dong, B., Deng, W. and Jiang, D. (2011). Distinct cytoskeleton populations and extensive crosstalk control *Ciona* notochord tubulogenesis. *Development* **138**, 1631–1641. doi:10.1242/dev.057208
- Effler, J. C., Kee, Y.-S., Berk, J. M., Tran, M. N., Iglesias, P. A. and Robinson, D. N. (2006). Mitosis-specific mechanosensing and contractile-protein redistribution control cell shape. *Curr. Biol.* **16**, 1962–1967. doi:10.1016/j.cub.2006.08.027
- Gilbert, S. F. and Barresi, M. J. F. (2016). *Developmental Biology*, 11th edn. Sinauer Associates.
- Gudipaty, S. A., Lindblom, J., Loftus, P. D., Redd, M. J., Edes, K., Davey, C. F., Krishnegowda, V. and Rosenblatt, J. (2017). Mechanical stretch triggers rapid epithelial cell division through Piezo1. *Nature* **543**, 118–121. doi:10.1038/nature21407
- Gutzman, J. H., Graeden, E. G., Lowery, L. A., Holley, H. S. and Sive, H. (2008). Formation of the zebrafish midbrain-hindbrain boundary constriction requires laminin-dependent basal constriction. *Mech. Dev.* **125**, 974–983. doi:10.1016/j.mod.2008.07.004
- Haigo, S. L., Hildebrand, J. D., Harland, R. M. and Wallingford, J. B. (2003). Shroom induces apical constriction and is required for hinge-point formation during neural tube closure. *Curr. Biol.* **13**, 2125–2137. doi:10.1016/j.cub.2003.11.054
- Hall, B. K. (1997). Phylotypic stage or phantom: is there a highly conserved embryonic stage in vertebrates? *Trends Ecol. Evol.* **12**, 461–463. doi:10.1016/S0169-5347(97)01222-6
- Hashimoto, H., Robin, F. B., Sherrard, K. M. and Munro, E. M. (2015). Sequential contraction and exchange of apical junctions drives zipper and neural tube closure in a simple chordate. *Dev. Cell* **32**, 241–255. doi:10.1016/j.devcel.2014.12.017
- Hertz, H. (1881). On the elastic contact of elastic solids. *J. Reine Angew. Math.* **92**, 156–171.
- Hibbitt, H., Karlsson, B. and Sorensen, E. (2011). *ABAQUS-Standard, User Manual, Version 10.1*. RI, USA: Inc., Pawtucket.
- Hotta, K., Mitsuhashi, K., Takahashi, H., Inaba, K., Oka, K., Gojobori, T. and Ikeo, K. (2007). A web-based interactive developmental table for the ascidian *Ciona intestinalis*, including 3D real-image embryo reconstructions: I. From fertilized egg to hatching larva. *Dev. Dyn.* **236**, 1790–1805. doi:10.1002/dvdy.21188
- Ikegami, S., Taguchi, T., Ohashi, M., Oguro, M., Nagano, H. and Mano, Y. (1978). Aphidicolin prevents mitotic cell division by interfering with the activity of DNA polymerase- α . *Nature* **275**, 458–460. doi:10.1038/275458a0
- Ikuta, T., Satoh, N. and Saiga, H. (2010). Limited functions of Hox genes in the larval development of the ascidian *Ciona intestinalis*. *Development* **137**, 1505–1513. doi:10.1242/dev.046938
- Jose-Edwards, D. S., Oda-Ishii, I., Nibu, Y. and Di Gregorio, A. (2013). Tbx2/3 is an essential mediator within the Brachyury gene network during *Ciona* notochord development. *Development* **140**, 2422–2433. doi:10.1242/dev.094227
- Kasza, K. E., Farrell, D. L. and Zallen, J. A. (2014). Spatiotemporal control of epithelial remodeling by regulated myosin phosphorylation. *Proc. Natl. Acad. Sci. USA* **111**, 11732–11737. doi:10.1073/pnas.1400520111
- Kondo, T. and Hayashi, S. (2013). Mitotic cell rounding accelerates epithelial invagination. *Nature* **494**, 125–129. doi:10.1038/nature11792
- Kuznetsova, T. G., Starodubtseva, M. N., Yegorenkov, N. I., Chizhik, S. A. and Zhdanov, R. I. (2007). Atomic force microscopy probing of cell elasticity. *Micron* **38**, 824–833. doi:10.1016/j.micron.2007.06.011
- Lappalainen, P. and Drubin, D. G. (1997). Cofilin promotes rapid actin filament turnover in vivo. *Nature* **388**, 78–82. doi:10.1038/40418
- Lee, J.-Y. and Goldstein, B. (2003). Mechanisms of cell positioning during *C. elegans* gastrulation. *Development* **130**, 307–320. doi:10.1242/dev.00211
- Lv, Z., Lu, Q. and Dong, B. (2019). Morphogenesis: a focus on marine invertebrates. *Mar. Life Sci. Technol.* **1**, 28–40. doi:10.1007/s42995-019-00016-z
- Mao, Y., Tournier, A. L., Hoppe, A., Kester, L., Thompson, B. J. and Tapon, N. (2013). Differential proliferation rates generate patterns of mechanical tension that orient tissue growth. *EMBO J.* **32**, 2790–2803. doi:10.1038/emboj.2013.197
- Marin-Riera, M., Moustakas-Verho, J., Savriama, Y., Jernvall, J. and Salazar-Ciudad, I. (2018). Differential tissue growth and cell adhesion alone drive early tooth morphogenesis: an ex vivo and in silico study. *PLoS Comput. Biol.* **14**, e1005981. doi:10.1371/journal.pcbi.1005981
- Martin, A. C., Kaschube, M. and Wieschaus, E. F. (2009). Pulsed contractions of an actin-myosin network drive apical constriction. *Nature* **457**, 495–499. doi:10.1038/nature07522
- Matsumura, K. D., Nakamura, M. J., Koizumi, W. C., Hotta, K. and Oka, K. (2020). Different strategies for tissue scaling in dwarf tailbud embryos revealed by single-cell analysis. *Dev. Biol.* **460**, 215–223. doi:10.1016/j.ydbio.2020.01.008
- Miller, S. A., Adornato, M., Briglin, A., Cavanaugh, M., Christian, T., Jewett, K., Michaelson, C., Monoson, T., Price, F., Tignor, J. et al. (1999). Domains of differential cell proliferation suggest hinged folding in avian gut endoderm. *Dev. Dyn.* **216**, 398–410. doi:10.1002/(SICI)1097-0177(199912)216:4<398::AID-DVDY8>3.0.CO;2-7
- Monier, B., Gettings, M., Gay, G., Mangeat, T., Schott, S., Guarner, A. and Suzanne, M. (2015). Apico-basal forces exerted by apoptotic cells drive epithelium folding. *Nature* **518**, 245–248. doi:10.1038/nature14152
- Munro, E. M. and Odell, G. M. (2002). Polarized basolateral cell motility underlies invagination and convergent extension of the ascidian notochord. *Development* **129**, 13–24.
- Nakano, K. and Mabuchi, I. (2006). Actin-depolymerizing protein Adf1 is required for formation and maintenance of the contractile ring during cytokinesis in fission yeast. *Mol. Biol. Cell* **17**, 1933–1945. doi:10.1091/mbc.e05-09-0900
- Negishi, T., Miyazaki, N., Murata, K., Yasuo, H. and Ueno, N. (2016). Physical association between a novel plasma-membrane structure and centrosome orients cell division. *eLife* **5**, e16550. doi:10.7554/eLife.16550
- Newman-Smith, E., Kourakis, M. J., Reeves, W., Veeman, M. and Smith, W. C. (2015). Reciprocal and dynamic polarization of planar cell polarity core components and myosin. *eLife* **4**, e05361. doi:10.7554/eLife.05361
- Nicolás-Pérez, M., Kuchling, F., Letelier, J., Polvillo, R., Wittbrodt, J. and Martínez-Morales, J. R. (2016). Analysis of cellular behavior and cytoskeletal dynamics reveal a constriction mechanism driving optic cup morphogenesis. *eLife* **5**, e15797. doi:10.7554/eLife.15797
- Nishimura, T., Honda, H. and Takeichi, M. (2012). Planar cell polarity links axes of spatial dynamics in neural-tube closure. *Cell* **149**, 1084–1097. doi:10.1016/j.cell.2012.04.021
- Oda-Ishii, I., Ishii, Y. and Mikawa, T. (2010). Eph regulates dorsoventral asymmetry of the notochord plate and convergent extension-mediated notochord formation. *PLoS ONE* **5**, e13689. doi:10.1371/journal.pone.0013689
- Ogura, Y., Sakaue-Sawano, A., Nakagawa, M., Satoh, N., Miyawaki, A. and Sasakura, Y. (2011). Coordination of mitosis and morphogenesis: role of a prolonged G2 phase during chordate neurulation. *Development* **138**, 577–587. doi:10.1242/dev.053132
- Ogura, Y. and Sasakura, Y. (2016). Developmental control of cell-cycle compensation provides a switch for patterned mitosis at the onset of chordate neurulation. *Dev. Cell* **37**, 148–161. doi:10.1016/j.devcel.2016.03.013
- Pasini, A., Amiel, A., Rothbacher, U., Roue, A., Lemaire, P. and Darras, S. (2006). Formation of the ascidian epidermal sensory neurons: insights into the origin of the chordate peripheral nervous system. *PLoS Biol.* **4**, e225. doi:10.1371/journal.pbio.0040225
- Poirier, C. C., Ng, W. P., Robinson, D. N. and Iglesias, P. A. (2012). Deconvolution of the cellular force-generating subsystems that govern cytokinesis furrow ingression. *PLoS Comput. Biol.* **8**, e1002467. doi:10.1371/journal.pcbi.1002467
- Segade, F., Cota, C., Famiglietti, A., Cha, A. and Davidson, B. (2016). Fibronectin contributes to notochord intercalation in the invertebrate chordate, *Ciona intestinalis*. *Evodevo* **7**, 21. doi:10.1186/s13227-016-0056-4
- Sehring, I. M., Dong, B., Denker, E., Bhattachan, P., Deng, W., Mathiesen, B. T. and Jiang, D. (2014). An equatorial contractile mechanism drives cell elongation but not cell division. *PLoS Biol.* **12**, e1001781. doi:10.1371/journal.pbio.1001781
- Sherrard, K., Robin, F., Lemaire, P. and Munro, E. (2010). Sequential activation of apical and basolateral contractility drives ascidian endoderm invagination. *Curr. Biol.* **20**, 1499–1510. doi:10.1016/j.cub.2010.06.075
- Shi, W., Peyrot, S. M., Munro, E. and Levine, M. (2009). FGF3 in the floor plate directs notochord convergent extension in the *Ciona* tadpole. *Development* **136**, 23–28. doi:10.1242/dev.029157
- Shi, Y., Yao, J., Young, J. M., Fee, J. A., Perucchio, R. and Taber, L. A. (2014). Bending and twisting the embryonic heart: a computational model for c-looping based on realistic geometry. *Front. Physiol.* **5**, 297. 10.3389/fphys.2014.00297
- Sidhaye, J. and Norden, C. (2017). Concerted action of neuroepithelial basal shrinkage and active epithelial migration ensures efficient optic cup morphogenesis. *eLife* **6**, e22689. doi:10.7554/eLife.22689
- Soiné, J. R. D., Brand, C. A., Stricker, J., Oakes, P. W., Gardel, M. L. and Schwarz, U. S. (2015). Model-based traction force microscopy reveals differential tension in cellular actin bundles. *PLoS Comput. Biol.* **11**, e1004076. doi:10.1371/journal.pcbi.1004076
- Sotiropoulos, A., Gineitis, D., Copeland, J. and Treisman, R. (1999). Signal-regulated activation of serum response factor is mediated by changes in actin dynamics. *Cell* **98**, 159–169. doi:10.1016/S0092-8674(00)81011-9
- Stemple, D. L. (2005). Structure and function of the notochord: an essential organ for chordate development. *Development* **132**, 2503–2512. doi:10.1242/dev.01812
- Tozluoglu, M., Duda, M., Kirkland, N. J., Barrientos, R., Burden, J. J., Muñoz, J. J. and Mao, Y. (2019). Planar differential growth rates initiate precise fold positions in complex epithelia. *Dev. Cell* **51**, 299–312.e4. doi:10.1016/j.devcel.2019.09.009
- Tuchmann-Duplessis, H., David, G. and Haegel, P. (1971). Flexion. In *Embryogenesis* (ed. H. Tuchmann-Duplessis G. David and P. Haegel), pp. 46–47. New York, NY: Springer New York.

- Veeman, M. T., Nakatani, Y., Hendrickson, C., Ericson, V., Lin, C. and Smith, W. C.** (2008). Chongmague reveals an essential role for laminin-mediated boundary formation in chordate convergence and extension movements. *Development* **135**, 33-41. doi:10.1242/dev.010892
- Vicente-Manzanares, M., Ma, X., Adelstein, R. S. and Horwitz, A. R.** (2009). Non-muscle myosin II takes centre stage in cell adhesion and migration. *Nat. Rev. Mol. Cell Biol.* **10**, 778-790. doi:10.1038/nrm2786
- von Baer, K. E.** (1928). *Entwicklungsgeschichte der Thiere: Beobachtung und Reflexion*. Königsberg: Bornträger.
- Wang, Y.-C., Khan, Z., Kaschube, M. and Wieschaus, E. F.** (2012). Differential positioning of adherens junctions is associated with initiation of epithelial folding. *Nature* **484**, 390-393. doi:10.1038/nature10938
- Zeller, R. W., Virata, M. J. and Cone, A. C.** (2006). Predictable mosaic transgene expression in ascidian embryos produced with a simple electroporation device. *Dev. Dyn.* **235**, 1921-1932. doi:10.1002/dvdy.20815
- Zhang, W. and Robinson, D. N.** (2005). Balance of actively generated contractile and resistive forces controls cytokinesis dynamics. *Proc. Natl. Acad. Sci. USA* **102**, 7186-7191. doi:10.1073/pnas.0502545102

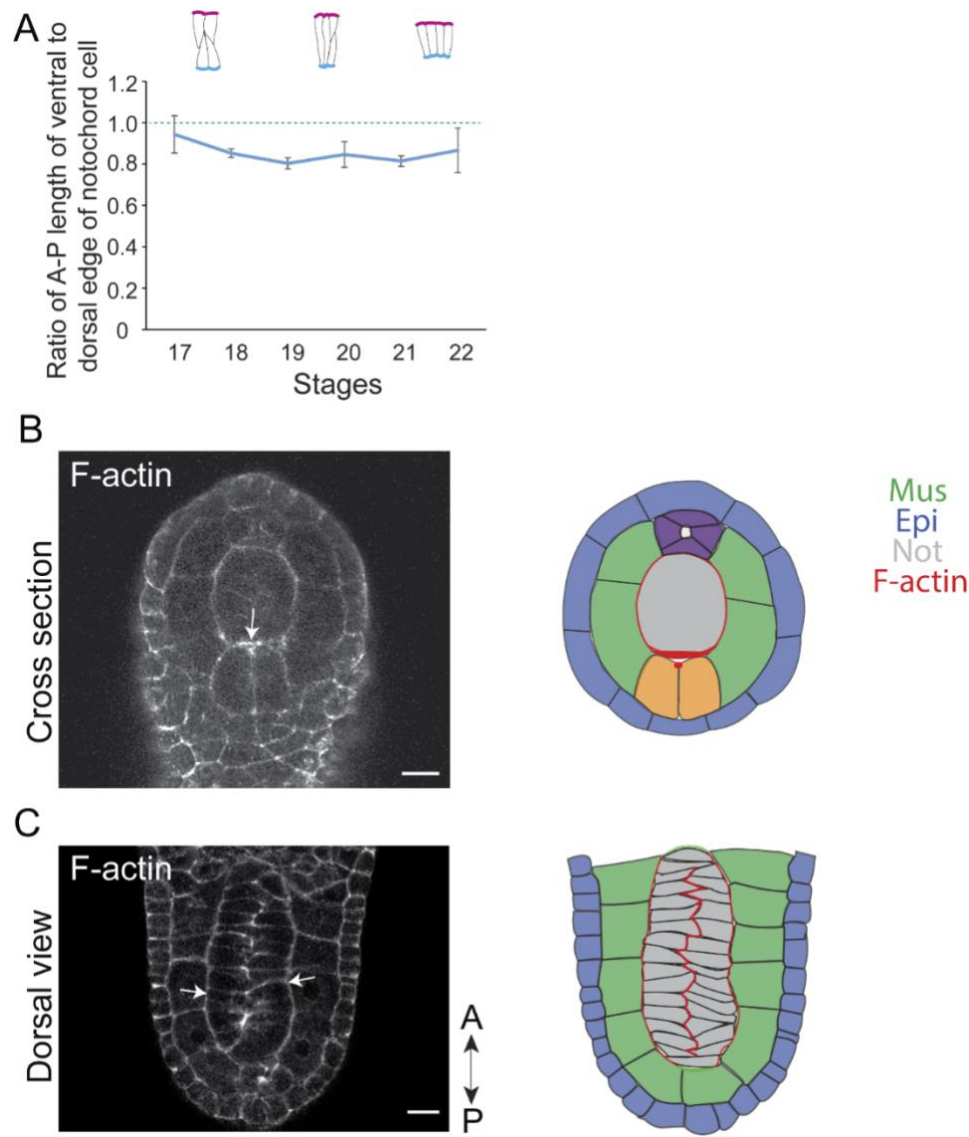


Fig. S1. The notochordal cells' geometry and F-actin in *Ciona* notochord. Related to Fig. 2. (A) Changes in notochordal cells' geometry by measuring the ratios of A-P length at dorsal and ventral edge of notochord cells in embryos at tailbud stages 17–22. Insets: notochordal cell shapes at tailbud stages 17, 19, and 21. Ratio = 1 is marked by a green dashed line. (B) Axial section of the notochord (left), highlighted in the drawings (right). Enriched F-actin at the notochord's ventral side (white arrows). Scale bar = 10 μ m. (C) Dorsal view of the notochord (left). Both left and right sides of the notochord (indicated by arrows) have relatively the same level of F-actin, summarized in the drawings (right). Scale bar = 10 μ m.

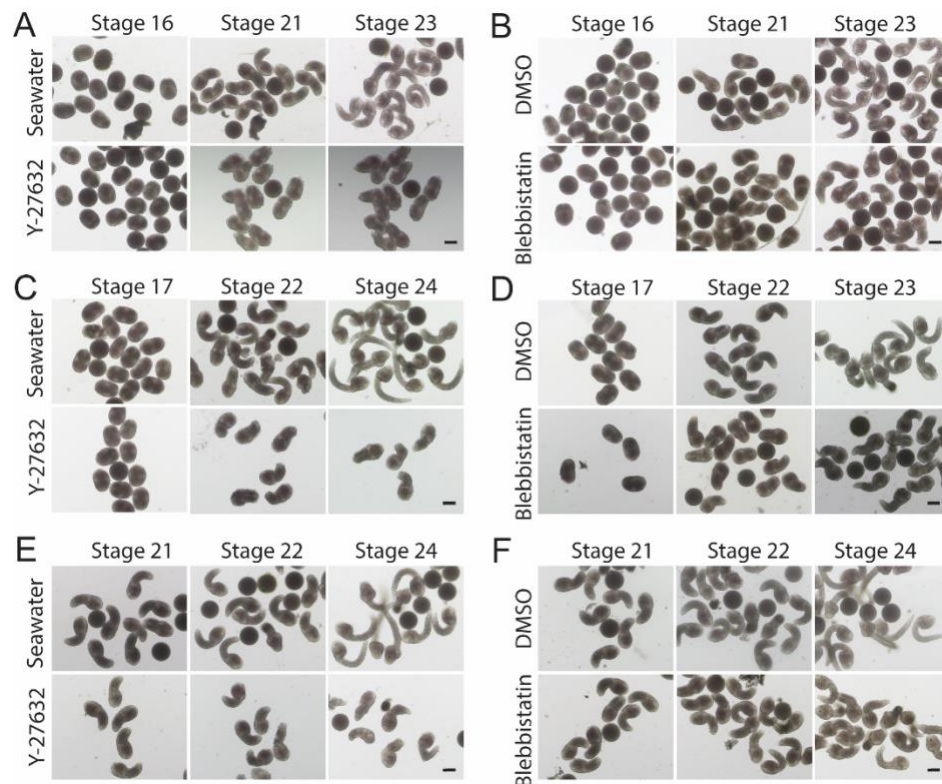


Fig. S2. Effects of drug treatment on embryonic tail bending in *Ciona robusta*. (A) Embryos' morphology before (left panel) and after the treatment with 200 μ M Y-27632 or seawater (control). Treatment started at tailbud stage 16 (16°C). Scale bar = 100 μ m. (B) Embryos' morphology before (left panel) and after the treatment with 100 μ M blebbistatin or DMSO (control). Treatment was started at tailbud stage 16 (16 °C). Scale bar = 100 μ m. (C) Embryos' morphology before (left panel) and after the treatment with 200 μ M Y-27632 or seawater (control). Treatment started at tailbud stage 17 (16°C). Scale bar = 100 μ m. (D) Embryos' morphology before (left panel) and after the treatment with 100 μ M blebbistatin or DMSO (control). Treatment started at tailbud stage 17 (16 °C). Scale bar = 100 μ m. (E) Embryos' morphology before (left panel) and after the treatment with 200 μ M Y-27632 or seawater (control). Treatment started at tailbud stage 21 (16°C). Scale bar = 100 μ m. (F) Embryos' morphology before (left panel) and after the treatment with 100 μ M blebbistatin or DMSO (control). Treatment started at tailbud stage 21 (16 °C). Scale bar = 100 μ m.

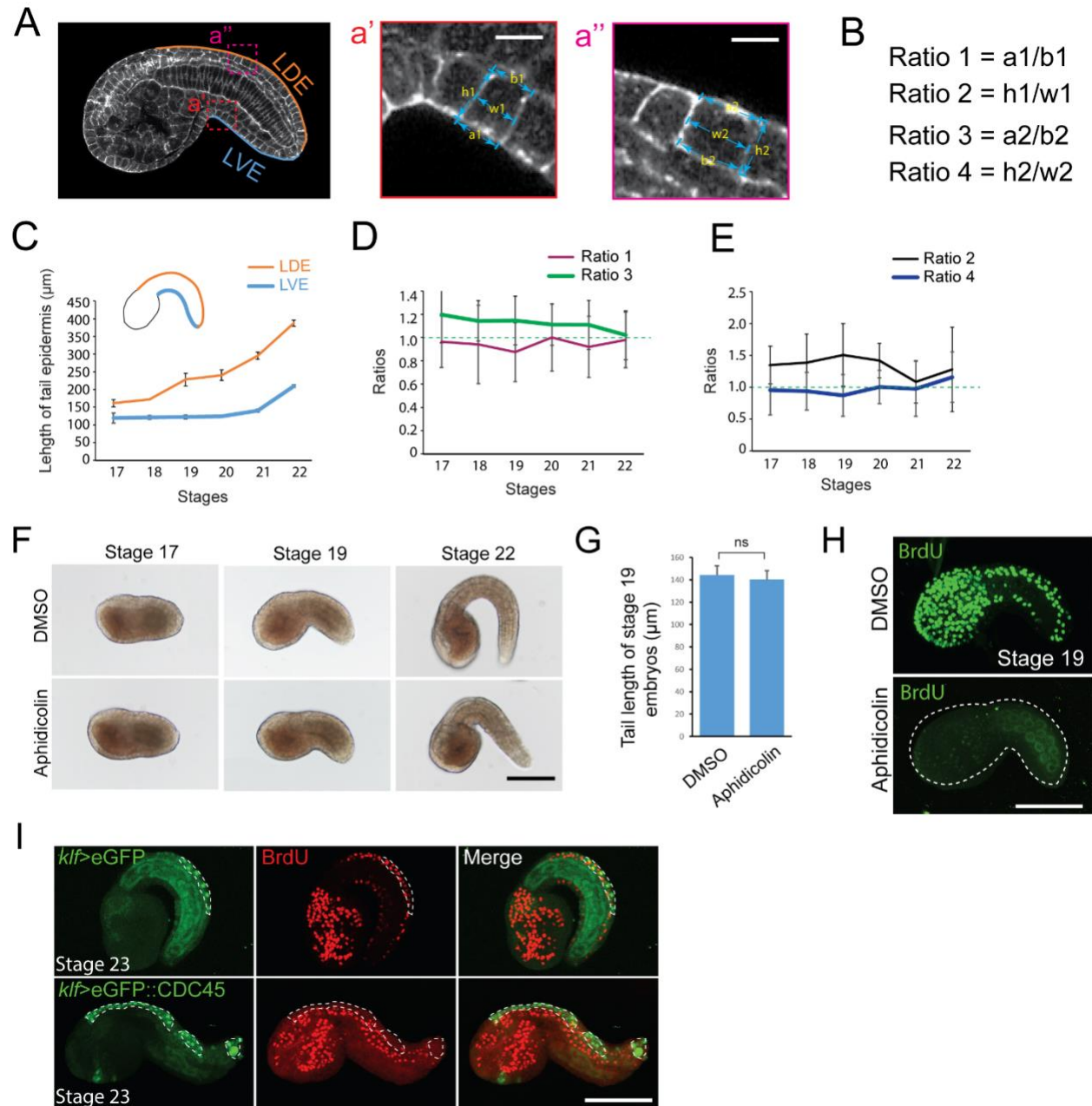


Fig. S3. Characterization of the role of epidermis during the embryonic tail bending in *Ciona robusta*. Related to Fig. 4. (A) Quantification of tail epidermal cell geometry in the basis of the confocal images. The embryos were stained by phalloidin. LDE, length of dorsal edge of embryo tail; LVE, length of ventral edge of embryo tail. Higher-magnification images of red- (a') and magenta-dashed (a'') box area. Scale bar = 10 μm . (B) Definition of ratios that describing the tail epidermis geometry (the corresponding

parameters are referred to A). (C) Changes in dorsal and ventral length of tail epidermis at tailbud stages 17–22. (D) Changes in ratios 1 and 3 at tailbud stages 17–22. Ratio = 1 is marked by a green dashed line. (E) Changes in ratios 2 and 4 at tailbud stages 17–22. Ratio = 1 is highlighted by a green dashed line. (F) DIC images displaying morphologies of DMSO- or aphidicolin-treated embryos at tailbud stages 17, 19, and 22. (G) Quantification of tail length of DMSO- (n = 31) or aphidicolin-treated (n=31) embryos at tailbud stage 19. (H) Confocal images (projection) showing distribution of BrdU-positive cells in DMSO- or aphidicolin-treated embryos at tailbud stage 17, 19, and 23. Scale bar = 100 μ m. (I) Confocal images (projection) showing distribution of BrdU-positive cells in *klf*>eGFP- and *klf*>eGFP :: *cdc45*- transfected embryos at tailbud stage 23. eGFP driven by *klf* promoter is expressed along the dorsal midline of epidermis (white dashed lines). Scale bar = 100 μ m.

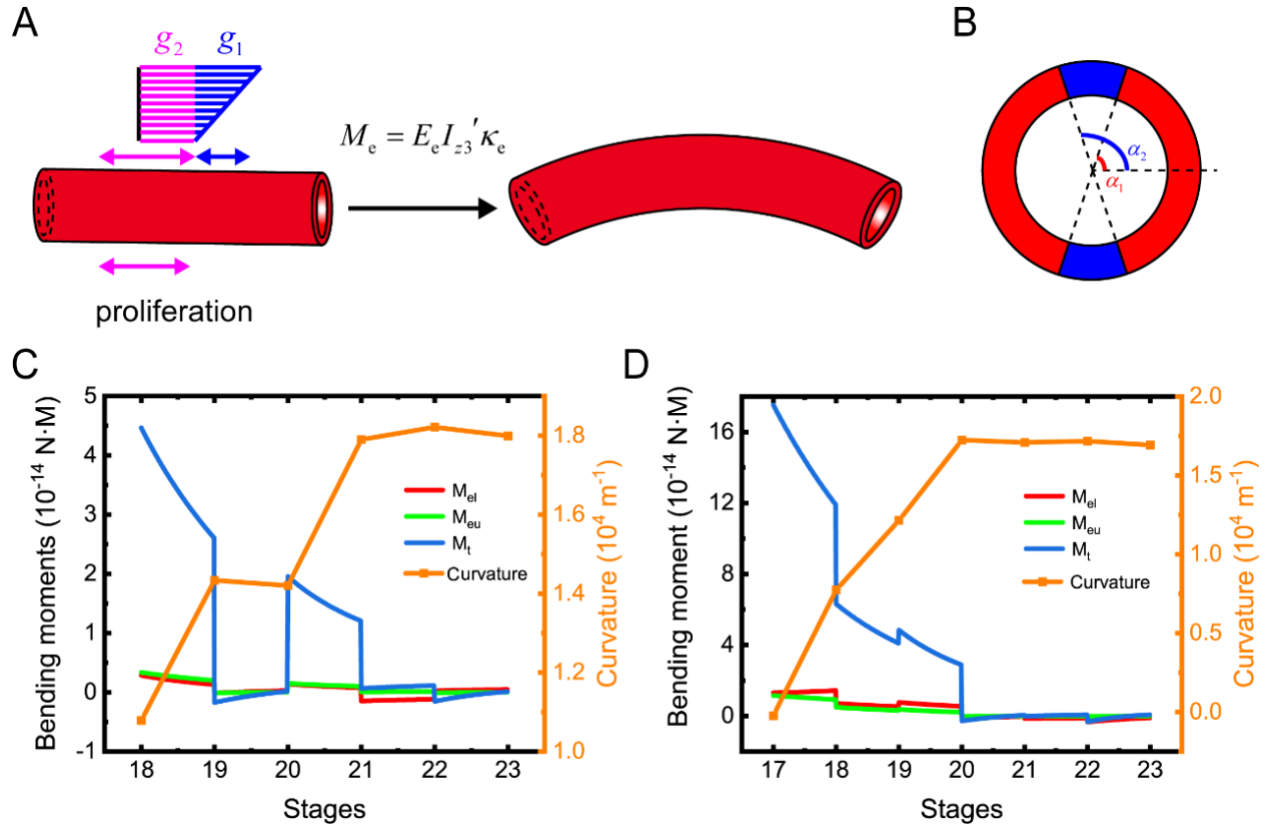


Fig. S4. Physical model for evaluating the contributions of notochord and epidermis during tail bending. (A) Gradient growth is used to simulate the volume change caused by differential epidermis proliferation. The growth of the epidermis can be divided into two parts, the differential part g_1 and the uniform part g_2 . (B) The cross section of the epidermis. The blue parts represent the dorsal and ventral epidermal cells undergoing mitosis. α_2 and α_1 are the polar coordinates of the cell boundaries. (C) and (D) show the bending moments induced by epidermis cell division, M_{el} and M_{eu} , and the total moment required to bend the tail for two typical embryos, M_t . The evolution of the curvature of the tail is also shown in (C) and (D).

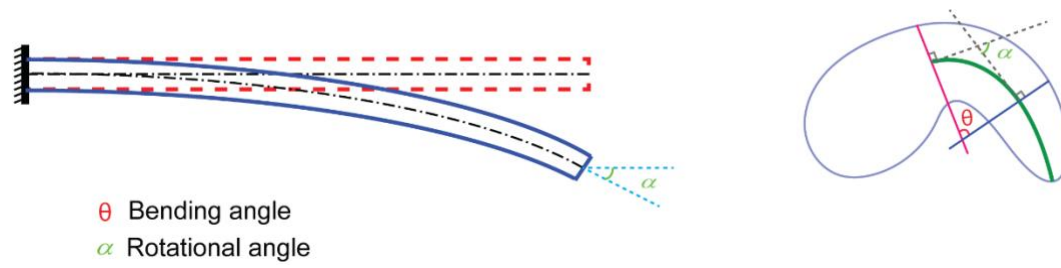


Fig. S5. The rotational and bending angle. The diagrams illustrate the definition of the rotational angle α and its relationship with bending angle θ .

Supplementary Materials and Methods

Physical model

To quantify the contribution of the notochord and epidermis to the tail bending, we proposed a composite beam model considering active processes (e.g., differential epidermis proliferation and notochord constriction) in the tail. The tail was theoretically treated as a cylindrical beam comprising three layers representing, from inside to outside, the notochord, muscle, and epidermis, respectively.

As the tail bends, dorsal epidermal cells proliferate faster than ventral ones. The effects of differential cell divisions may be divided into two portions: cell divisions may enlarge the total volume of the epidermis and further bend the tail; and cell divisions along the anteroposterior (AP) axis may actively elongate the cells along the AP axis, shortening the cell width correspondingly.

First, we evaluated the effect of cell volumes enlargement. In this case, we neglected the possibility that cell divisions along the AP axis may actively elongate the cells along the AP axis. Gradient growth was used to simulate the volume change caused by differential epidermis proliferation, as shown in Fig. S4A. Epidermis growth expansion was restricted to the axial direction. The growth of the epidermis can be divided into two parts, the differential part g_1 and the uniform part g_2 . The differential growth strain, denoted by g_1 , induces a spontaneous curvature

$$\kappa_e = \frac{g_1}{d_3}. \quad (\text{S1})$$

As the epidermis proliferates, the restraint by the notochord and muscle can create a relatively high stress in the tail. The bending moment M_e due to the differential proliferation of the epidermis can be calculated by

$$M_e = E_e I_{z3}' \kappa_e, \quad (\text{S2})$$

where I'_{z3} is the moment of inertia for the dorsal and ventral epidermis undergoing differential cell division and is given by

$$I'_{z3} = \frac{d_3^4 - d_2^4}{64} \left(\alpha_2 - \alpha_1 - \frac{\sin 2\alpha_2 - \sin 2\alpha_1}{2} \right), \quad (\text{S3})$$

where α_2 and α_1 are the polar coordinates of the cell boundaries, as shown in Fig. S4B. Substituting Eqs. (S1) and (S3) into Eq. (S2), we get

$$M_e = \frac{d_3^4 - d_2^4}{32d_3} \left(\frac{\alpha_2 - \alpha_1}{2} - \frac{\sin 2\alpha_2 - \sin 2\alpha_1}{4} \right) E_e g_1. \quad (\text{S4})$$

where g_1 is the amount of differential tissue growth. According to the volume growth theory, g_1 is given by

$$g_1 = \frac{\Delta L_e}{L}, \quad (\text{S5})$$

where ΔL_e is the differential length between the dorsal and ventral sides of the epidermis because of differential epidermis proliferation. The observed differential length between the dorsal and ventral sides of the epidermis, ΔL_{em} , is due to both epidermis differential proliferation and notochord constriction. The observed differential length ΔL_{em} can be divided into two parts: the differential length $\Delta L'_e$ due to elastic deformation (the contraction of the notochord) and the differential length ΔL_e due to differential proliferation, $\Delta L_{em} = \Delta L_e + \Delta L'_e$. $\Delta L'_e$ can be obtained as follows. First, when the epidermis proliferation is neglected, the epidermis is assumed as incompressible and the volume of epidermis is conserved for different stages. Then, we can calculate the change of length $\Delta L'_e$ from the changes in the epidermis height and width measured from experiments. Substituting ΔL_e into Eq. (S5) and then into Eq. (S4), we obtain the contribution of differential cell divisions due to the change of volume, M_{el} .

Secondly, we considered the condition that cell divisions along the AP axis may actively elongate the cells along the AP axis and thus bend the tail. During the tail bending, the elongation of the notochord may also stretch and elongate the epidermal cells along the AP axis. Therefore, it is hard to distinguish the contributions of these two mechanisms to the length change. In this part, we considered an extreme situation: the elongation of the epidermis along the AP axis is totally caused by cell division, i.e., the notochord does not stretch the epidermis. In this vein, the observed differential length ΔL_{em} is fully caused by differential cell divisions. Substituting ΔL_{em} into Eq. (S5) and then into Eq. (S4), we obtain an estimate of the contribution of differential cell divisions, M_{eu} .

During embryonic tail bending, F-actin and myosin II asymmetrically assemble at the notochord's ventral side, causing notochord constriction. The bending moment produced by the contractile force M_n is hard to calculate directly, since the underlying mechanisms of actomyosin constriction are complex and difficult to measure. Therefore, an indirect approach is utilized. First, the total moment required to bend the whole tail is calculated as

$$M_t = EI_z \kappa_t, \quad (S6)$$

where EI_z is the bending stiffness of the tail and is given by

$$EI_z = \frac{E_n \pi d_1^4}{64} + \frac{E_m \pi d_2^4}{64} \left(1 - \frac{d_1^4}{d_2^4} \right) + \frac{E_e \pi d_3^4}{64} \left(1 - \frac{d_2^4}{d_3^4} \right), \quad (S7)$$

where E_m and E_e are Young's modulus of the muscle and epidermis, respectively; I_z is the moment of inertia; and κ_t is the curvature of the tail. Then the bending moment caused by the contraction of notochord M_n can be calculated by $M_n = M_t - M_e$.

Using the representative values of the parameters given in Fig. 5 and Table S1, the bending moments M_{el} , M_{eu} and M_t were calculated for different stages for two typical embryos (Figs. S4C,D). The curvatures of the tail were calculated to depict the bending process. It is shown that at tailbud stages ~17–20/21 the curvature increases and the tail bends gradually, while at the tailbud stages ~20/21–23 the curvature is almost unchanged and the tail does not bend further, though the length of the tail continues to increase. Accordingly, the total moment M_t is positive for the early stages, while M_t falls to close to zero at the late stages. It is shown that the bending moment induced by the differential cell division of epidermis, M_{el} and M_{eu} , is relatively tiny compared to the total bending moment M_t . In this vein, we concluded that the contribution of the epidermis to the tail bending is dispensable, which is also confirmed by our experiments.

It was worth to note that in the above calculations, the geometric parameters of the same embryo for different stages were used. The precise values of the geometric parameters are difficult to obtain, therefore the DIC images of the embryo are used which may lead to some errors of the data. Though the value of the bending moments may be not quite accurate, the underlying mechanisms are conserved. Furthermore, the results show that the bending moment caused by the differential epithelial proliferation is pretty small, we believe that the limited errors of the data cannot change the conclusion that the contribution of epithelial proliferation is dispensable.

Table S1. Geometric measurements of the staged 17–22 *Ciona* embryos.

| | Items | Stage 17 | Stage 18 | Stage 19 | Stage 20 | Stage 21 | Stage 22 |
|----------------|--|----------------|----------------|----------------|----------------|----------------|----------------|
| Embryo | A-P length of the embryo | 215.87 ± 9.50 | 230.84 ± 7.94 | 277.86 ± 10.10 | 287.37 ± 12.53 | 330.93 ± 22.53 | 397.18 ± 19.25 |
| | A-P length of the tail | 126.42 ± 5.36 | 135.73 ± 9.12 | 170.02 ± 2.17 | 181.59 ± 10.71 | 221.99 ± 6.43 | 277.07 ± 26.84 |
| Notochord | A-P length of the dorsal edge of the notochord | 121.29 ± 6.21 | 143.06 ± 6.83 | 165.21 ± 1.72 | 186.31 ± 14.52 | 235.68 ± 12.84 | 283.28 ± 25.28 |
| | Average diameter of the spherical notochord | -- | 38.43 ± 4.36 | 36.14 ± 5.94 | 31.22 ± 4.79 | 27.00 ± 1.16 | 23.98 ± 3.30 |
| | Number of notochordal cell occupied along the dorsal edge of notochord | ~18 | ~22 | ~27 | ~35 | 40 | 40 |
| | A-P length of the ventral edge of the notochord | 106.42 ± 11.09 | 116.87 ± 12.29 | 131.79 ± 12.30 | 147.51 ± 18.02 | 181.98 ± 11.87 | 245.49 ± 29.87 |
| | Number of notochordal cell occupied along the ventral edge of notochord | ~17 | ~21 | ~27 | ~33 | 40 | 40 |
| | Average A-P length of notochord cell (along the dorsal edge) | 6.51 ± 0.53 | 6.44 ± 0.65 | 6.15 ± 1.19 | 5.25 ± 0.34 | 6.06 ± 0.77 | 7.60 ± 0.79 |
| | Average A-P length of notochord cell (along the ventral edge) | 6.11 ± 0.41 | 5.40 ± 0.51 | 4.93 ± 0.91 | 4.44 ± 0.41 | 4.93 ± 0.67 | 6.59 ± 1.21 |
| Tail epidermis | A-P length of dorsal midline of tail epidermis | 161.41 ± 10.58 | 172.26 ± 0.46 | 228.20 ± 17.63 | 240.50 ± 14.72 | 295.32 ± 22 | 387.06 ± 39.26 |
| | Average A-P length of dorsal midline of tail epidermal cell (apical domain) | 13.623 ± 3.82 | 10.60 ± 2.23 | 11.72 ± 2.86 | 9.66 ± 1.66 | 9.92 ± 2.46 | 8.62 ± 2.3 |
| | Average D-V length of dorsal midline of tail epidermal cell | 12.06 ± 3.24 | 10.84 ± 1.77 | 9.35 ± 2.43 | 9.09 ± 1.92 | 8.56 ± 1.98 | 9.01 ± 1.73 |
| | Cell number of dorsal midlines of tail epidermis (section) | ~ 11 | ~ 17 | ~ 20 | ~ 28 | ~ 38 | ~ 45 |
| | A-P length of ventral midline of tail epidermis | 119.53 ± 14.13 | 121.24 ± 5.70 | 122.48 ± 5.06 | 123.86 ± 0.63 | 140.45 ± 8.81 | 209.51 ± 40.81 |
| | Average A-P length of ventral midline of tail epidermal cell (apical domain) | 10.52 ± 2.54 | 9.54 ± 3.66 | 6.9 ± 2.4 | 7.63 ± 2.11 | 8.28 ± 1.56 | 6.96 ± 3.06 |
| | Average D-V length of ventral midline of tail epidermal cell | 14.33 ± 2.94 | 12.92 ± 2.28 | 10.84 ± 1.68 | 10.96 ± 1.26 | 9.22 ± 1.22 | 9.61 ± 1.79 |
| | Cell number of ventral midlines of tail epidermis (section) | ~ 10 | ~ 12 | ~ 16 | ~ 16 | ~ 20 | ~ 30 |



Movie 1. Time-lapse movie shows the development of *Ciona* embryo within chorion.

Movie duration is for 2.72 h, and is shown at 100 frames per second. Shown as stills in Fig. 1A. Scale bar = 50 μ m.



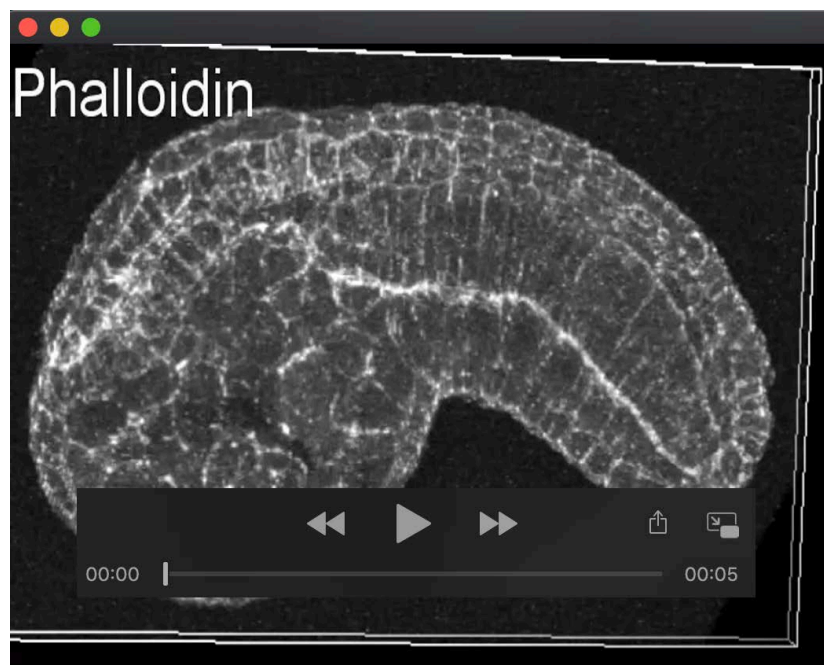
Movie 2. Time-lapse movie shows the development of the dechorionated *Ciona* embryo.

Movie duration is for 1.75 h, and is shown at 100 frames per second. Shown as stills in Fig. 1A. Scale bar = 50 μ m.



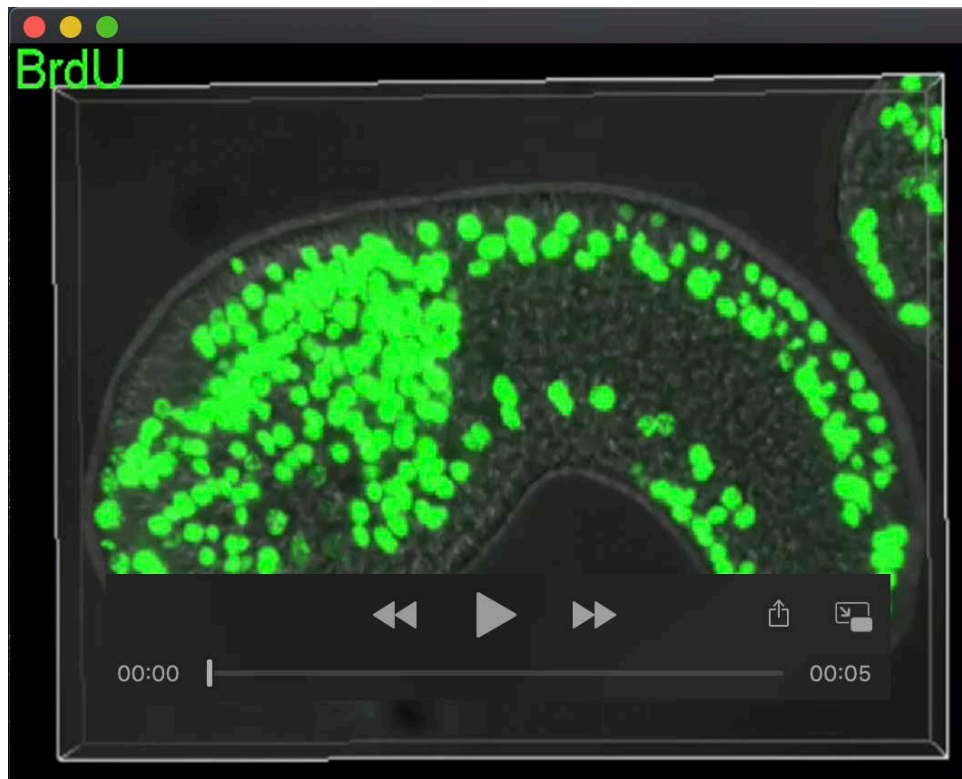
Movie 3. Time-lapse movie shows the development of the cutting tail.

Movie duration is for 1.91 h, and is shown at 100 frames per second. Shown as stills in Fig. 1D. Scale bar = 50 μ m.



Movie 4. 3D rendering movie from confocal image of the phalloidin-stained embryo at tailbud stage 19.

Embryo is stained with 1/200 Alexa Fluor® 488-conjugated phalloidin.



Movie 5. 3D rendering movie from confocal images of the BrdU-stained embryo at tailbud stage 19.

BrdU-positive cells (green) are merged with DIC image of the same embryo.